Whole-Ecosystem Experiment Illustrates Short Timescale Hydrodynamic, Light, and Nutrient Control of Primary Production in a Terminal Slough

Luke C. Loken[1,2] · Steven Sadro[2] · Leah E. K. Lenoch[3] · Paul R. Stumpner[3] · Randy A. Dahlgren[4] · Jon R. Burau[3] · Erwin E. Van Nieuwenhuyse[5]

Abstract

Estuaries are among the most productive of aquatic ecosystems. Yet the collective understanding of patterns and drivers of primary production in estuaries is incomplete, in part due to complex hydrodynamics and multiple controlling factors that vary at a range of temporal and spatial scales. A whole-ecosystem experiment was conducted in a deep, pelagically dominated terminal channel of the Sacramento-San Joaquin Delta (California, USA) that seasonally appears to become nitrogen limited, to test whether adding calcium nitrate would stimulate primary productivity or increase phytoplankton density. Production did not respond consistently to fertilization, in part because nitrate and phytoplankton were dispersed away from the manipulated area within 1–3 days. Temporal and spatial patterns of gross primary production were more strongly related to stratification and light availability (i.e., turbidity) than nitrogen, highlighting the role of hydrodynamics in regulating system production. Similarly, chlorophyll was positively related not only to stratification but also to nitrogen—with a positive interaction—suggesting stratification may trigger nutrient limitation. The average rate of primary production (4.3 g O_2 m^{-2} d^{-1}), metabolic N demand (0.023 mg N L^{-1} d^{-1}), and ambient dissolved inorganic nitrogen concentration (0.03 mg N L^{-1}) indicate that nitrogen can become limiting in time and space, especially during episodic stratification events when phytoplankton are isolated within the photic zone, or farther upstream where water clarity increases, dispersive flux decreases, and stratification is stronger and more frequent. The role of hydrodynamics in organizing habitat connectivity and regulating physical and chemical processes at multiple temporal and spatial scales is critical for determining resource availability and evaluating biogeochemical processes in estuaries.

Keywords Estuary · Nutrients · Light · Metabolism · Hydrodynamics · Phytoplankton · Ecosystem management

---

✉ Luke C. Loken
lloken@usgs.gov

1   U.S. Geological Survey, Upper Midwest Water Science Center, Middleton, WI, USA

2   Department of Environmental Science and Policy, University of California-Davis, Davis, CA, USA

3   U.S. Geological Survey, California Water Science Center, Sacramento, CA, USA

4   Department of Land, Air, and Water Resources, University of California-Davis, Davis, CA, USA

5   Bureau of Reclamation, Science Division, Bay-Delta Office, Sacramento, CA, USA

Introduction

Estuaries are among the most productive of aquatic ecosystems (Hoellein et al. 2013). Hydrological connectivity between rivers and the ocean drives heterogeneity in numerous physical and chemical properties, creating a myriad of habitats in which rates of primary and secondary production are elevated as a result of organic matter and nutrient inputs from freshwater and marine sources (Kelly and Levin 1986; Hopkinson and Smith 2005; Cloern et al. 2014). It is fairly well understood that variation in nutrients, light, and water clarity in estuaries drive spatial and temporal variability in primary production (Boynton et al. 1982; Jassby et al. 2002; Cloern et al. 2014), relations that are broadly consistent with observations from other aquatic systems (Hoellein et al. 2013; Solomon et al. 2013; Bernhardt et al. 2018). However,

whereas variation in drivers of primary production at short timescales have been thoroughly explored in lotic and lentic waters, similar studies in estuaries have lagged (Hoellein et al. 2013; Murrell et al. 2018; Wang et al. 2018; Loken et al. 2021), in part because of their high degree of habitat heterogeneity and complex tidal hydrodynamics (Kemp and Boynton 1980; Cloern et al. 1983; Cloern 1996; Beck et al. 2015; Lenoch et al. 2021a).

Production in estuaries may have multiple controls that vary spatially and temporally in accordance with hydrodynamic variability, including tidal strength, wind, and riverine inputs (Cloern 1996; Ragueneau et al. 1996; Yin et al. 1997; Mallin et al. 1999; Lucas et al. 2006). Advective and dispersive processes establish gradients in nutrients and turbidity, regulating both phytoplankton exposure to light and uptake potential of nitrogen (N) and phosphorus (P) (Kemp and Boynton 1984; Koseff et al. 1993; Sin et al. 1999; Yin and Harrison 2000; Wang et al. 2021). Where water exchange rates are high, nutrient availability may be high due to short water turnover times, yet light availability in these locations can be low due to high turbidity (Mallin et al. 1999; Domingues et al. 2011; Xu et al. 2012; Cloern et al. 2016). Spatial heterogeneity within estuaries allows for light to be more available and nutrients to be more limiting in terminal sloughs and other off-channel habitats, where exchange rates of water are lower (Powell et al. 1989; Bernhard and Peele 1997; Downing et al. 2016; Stumpner et al. 2020a).

The factors governing primary production in terminal channels, where water exchange rates are low and age of water increases, are complex (Lopez et al. 2006; Cloern 2007; Downing et al. 2016), with important implications for energetic source—sink dynamics within the ecosystem (Malone et al. 1986; Crosswell et al. 2017; Wang et al. 2018). Despite their historic loss, terminal sloughs, with their habitat complexity, continue to provide important contributions to the food web for pelagic consumers in estuaries (Carle et al. 2020; Young et al. 2020). Although these habitats can support higher phytoplankton abundance than areas with faster water exchange rates (Stumpner et al. 2020a), the extent to which nutrient limitation may play a role in regulating phytoplankton remains unclear, especially in the context of transport processes that can be dominated by tidal hydrodynamics that vary at short timescales. While the complexities of hydrodynamics are often acknowledged, fundamental questions about the processes involved, the timescales and conditions under which they operate, and the mechanistic implications for rates of primary production are rarely empirically tested.

Herein, we evaluated short timescale variations in drivers of primary production and chlorophyll *a* (Chl *a*) biomass in a terminal slough within the Sacramento-San Joaquin Delta where hydrological connectivity is limited and varies along a landward gradient (Downing et al. 2016; Feyrer et al. 2017;

Stumpner et al. 2020b). The experiment broadly asks the following: (1) does N become limiting to primary production in this terminal slough? (2) how often and under what conditions do tidal hydrodynamics mediate nutrient limitation? and (3) what are the relevant timescales involved? We characterized the availability of light and nutrients within the system to establish seasonal variations in potential controls on primary production and demonstrated N limitation of phytoplankton production through laboratory bioassays. After identifying when and where N appeared limiting in the system (dissolved inorganic nitrogen (DIN) < 0.03 mg N L^{-1}), we conducted a whole-ecosystem experiment where calcium nitrate was applied and monitored within a 7-km reach over a 2-month period (Table S1). Opportunities for such whole-system manipulations are rare but have yielded valuable insight into mechanistic controls of primary production in both marine and freshwater systems (Martin et al. 1994; Carpenter et al. 1995; Boyd et al. 2000; Schindler et al. 2008). Following our whole-ecosystem manipulation, we measured temporal and spatial variation in stratification, dispersion (Lenoch et al. 2021a), phytoplankton/zooplankton abundance, nutrient concentrations, and water clarity, all of which influence ecosystem energetics, which we characterized by modeling metabolic rates (Loken et al. 2021). Understanding the linkages between hydrodynamics and controls of primary production is critical for guiding future management actions aimed at increasing food supply for delta fish populations (Frantzich et al. 2021; Hartman et al. 2021) and, more generally, for improving understanding of coupled physical-biogeochemical dynamics in estuaries.

Methods

Site Description

The Sacramento-San Joaquin Delta (California, USA; hereafter "the delta") is the landward and predominantly freshwater part of the largest estuary on the Pacific Coast of North America. The delta has a long history of environmental and hydrologic alterations that have resulted in overall low productivity and declines among many pelagic organisms (Sommer et al. 2007; Van Nieuwenhuyse 2007; Lund et al. 2010; Cloern et al. 2011; Whipple et al. 2012; Marineau and Wright 2014; Healey et al. 2016). Most of the historic off-channel wetland areas are farmed, and natural waterways have been replaced by a network of mostly narrow, deep, and rocked conveyance canals (Robinson et al. 2014; Cloern et al. 2016). Along with introduced species, these physical changes have contributed to the delta's comparatively low productivity.

The Sacramento River Deep Water Ship Channel (DWSC) is one of the few remaining deep, off-channel habitats of the delta. The DWSC was constructed in 1963 to allow oceangoing

ships passage to the Port of West Sacramento (Fig. 1). The DWSC is approximately 40 km long and 150 m wide, has a mean depth of 7.5 m, and has minimal peripheral shallow-water habitat (Fregoso et al. 2020). The entire DWSC is tidal, where water levels fluctuate up to 2 m daily. A set of decommissioned locks connects the northern terminus of the DWSC to the Sacramento River. The DWSC lacks stream inputs, and although some water leaks through the locks during periods of high river flow, net flows in the DWSC are minimal (Lenoch et al. 2021a). Water originating from the lower Sacramento

River and Cache Slough Complex floods into the lower DWSC during each tide cycle, gradually dispersing landward. Functionally, the system resembles a dead-end slough with a straight and homogeneous channel for most of its length.

While the physical dimensions of the DWSC appear uniform, multiple physical and chemical gradients exist along the DWSC longitudinal axis driven primarily by hydrodynamics. During each low tide, the majority of the water volume remains in the DWSC, but some fraction of the water in the lower portion of the DWSC exchanges with the greater delta. The
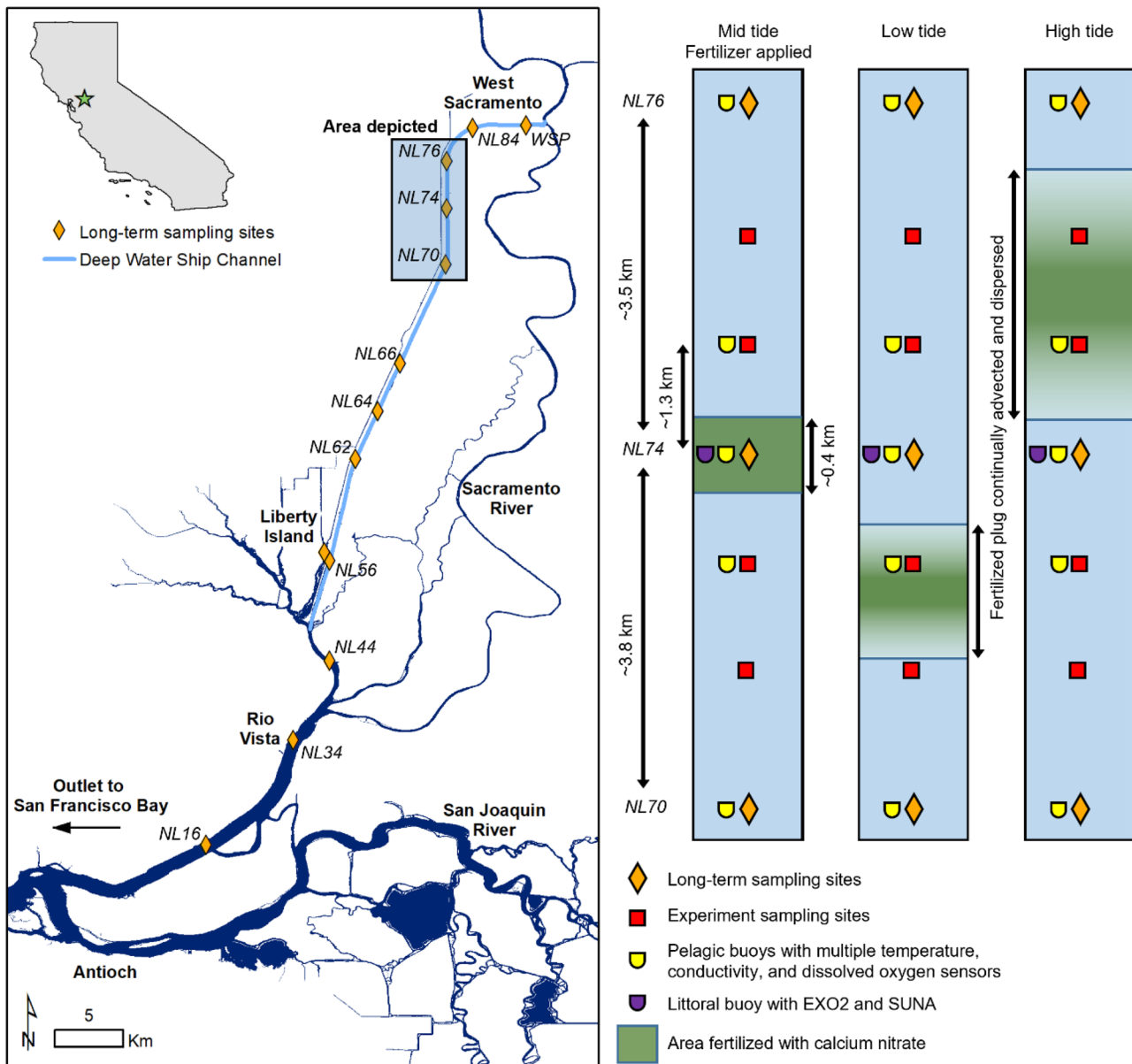
Fig. 1 Location of Sacramento River Deep Water Ship Channel, long-term sampling sites (left), and sampling design during the experiment (right). Fertilizer was applied each day to a 0.4-km segment (green polygon) centered at the long-term sampling site (NL74). Based on hydrodynamics, the fertilized water mass could be seaward or landward of NL74, moving up to 4 km daily due to tides (excursion length). Sensor arrays (half-ovals) were deployed ~30 from the western shore. Synoptic sampling occurred in the center of the channel at 7 sites (orange diamonds and red squares) evenly spaced longitudinally. Note the inset not drawn to scale

location of the boundary between the "mixed" and "persisting" water masses continually changes with the strength and phasing (i.e., ebb and flood) of the tides (Stumpner et al. 2020b). Moving landward from this Lagrangian habitat boundary, tidal energy dampens and the DWSC becomes increasingly isolated from the rest of the delta. Through evaporation, water isotope ratios (δ^2H, δ^{18}O) and specific conductivity (SPC) gradually increase landward (Figs. S1 and S2), both of which are proxies for relative water age (Downing et al. 2016; Gross et al. 2019). Water in the upper channel is older and exchanges with seaward environments more slowly (Lenoch et al. 2021a), whereas the lower channel has faster water velocities and has greater rates of water exchange. Spatial patterns in turbidity, N availability, and tidal dispersion create a gradient of generally increasing water clarity and decreasing DIN landward from the turbidity maximum (Feyrer et al. 2017) (Fig. S1).

Characterizing Nutrient Limitation

Long-term water chemistry and laboratory incubations were used to assess the potential of nutrient limitation in the DWSC. Physical, chemical, and biological properties at 13 sites between Antioch and West Sacramento, CA were sampled ~ monthly between 2012 and 2019 (Fig. 1). Here, we present turbidity, Secchi depth, SPC, N and P concentrations, Chl *a*, phytoplankton biovolume, and zooplankton biomass (see Fig. S1). Given comparatively high P concentrations, N was considered potentially limiting when DIN was below 0.03 mg N L^{-1} as typically occurred during the summer months landward of station NL74 (Fig. S3). While this concentration threshold is somewhat arbitrary, it is near the analytical detection level in this study (0.01 mg N L^{-1}) and ~ 25% of the average unconstrained N demand estimated based on laboratory incubations (Table S2).

Bioassay incubations were used to directly test for nutrient limitation starting in May 2018 by modeling pelagic metabolic rates using changes in dissolved oxygen (DO). A total of 6 L of surface water (~ 1 m depth, passed through a 150-μm screen to remove zooplankton) was collected from four sites (NL34, NL64, NL70, and NL74) on nine dates between May 2018 and May 2019. Water was stored at ambient temperature in the dark for no more than 8 h prior to dividing into three treatments, consisting of a control (no amendment), + N (amended with NO$_3$-N raising concentrations by 1 mg N L^{-1}), and + NP (amended with NO$_3$-N and PO$_4$-P raising the concentrations by 1 mg N L^{-1} and 0.15 mg P L^{-1}). Amendment concentrations are slightly above the observed long-term maxima (Fig. S3). Water from each site/treatment was distributed into 3–4 replicate borosilicate glass jars (~ 500 mL volume) that had a PreSens (www.presens. de) optical DO sensor installed. Jars were equilibrated in the dark for 12 h before the start of the experiment, after which they were exposed to 12 h of light at irradiance levels (300–330 μM m^2 s^{-1} photosynthetically active radiation

(PAR)) to measure net ecosystem production (NEP) and 12 h in the dark to measure ecosystem respiration (ER; reported as a negative number) repeatedly over the course of 4 days. Gross primary production (GPP) was computed as the difference of NEP and ER. Details of the method are described in Loken et al. (2021). Differences between the control and nutrient-amended incubations were used to assess the potential for nutrient limitation.

Nitrogen Amendment Experiment

Our whole-ecosystem, reach-scale nutrient amendment experiment was done in a portion of the DWSC with confirmed potential for N limitation of phytoplankton production (Figs. 1 and 2). During the summer of 2019, we added nitrate (NO$_3$) to the channel (centered at NL74) in July and August when DIN concentrations were near their annual minimum (Fig. S3). The goal of the experiment was to elevate NO$_3$ concentrations for at least five consecutive days to characterize short timescale variations in ecosystem metabolism, phytoplankton and zooplankton abundances, and other ecosystem properties. Because of tidal currents, NO$_3$ applications needed to occur repeatedly (consecutive days) to counter the effects of dispersion (Lenoch et al. 2021a). We fertilized during neap tide, when tidal currents and dispersion are weaker, to maximize the persistence of NO$_3$ within the fertilized area. We conducted two 4-day applications (Fig. 3, Table S1) on consecutive neap tides (i.e., 14 days apart).

On each of the eight fertilization days, we applied 1361 kg (211 kg NO$_3$-N) of commercially available granular calcium nitrate (YaraLiva Calcinit—Yara, Tampa, FL) to a 400-m segment (~ 60,000 m^2) of the channel centered at the long-term NL74 sampling site (38.5064° N, 121.5847° W; Fig. 1). We applied the fertilizer using a crop-dusting airplane (Fig. S4) to achieve a fast (< 30 min) and homogeneous application, aimed at raising NO$_3$ concentrations by 0.4 mg N L^{-1} (the approximate long-term maximum at NL74, Fig. S3) throughout the water column within the fertilized area. Immediately following each application, we mapped surface concentrations using a boat-mounted flow-through system and collected water samples from multiple depths and locations (see the "Sampling Methods" section) to confirm that concentrations increased within the targeted area and the fertilizer fully dissolved in the upper portion of the water column.

We monitored numerous physical, chemical, and biological metrics for 1 month before and after each fertilization for a total duration of 2 months (Fig. 3). Given the dispersion and timescales of mixing (Lenoch et al. 2021a), we collected discrete samples daily (Mon to Fri) for a week after each fertilization. We monitored the preceding and succeeding neap tides at the same frequency, using these two time periods as controls and to document short timescale variability. Because neap tides occur every ~ 14 days, these 5-day
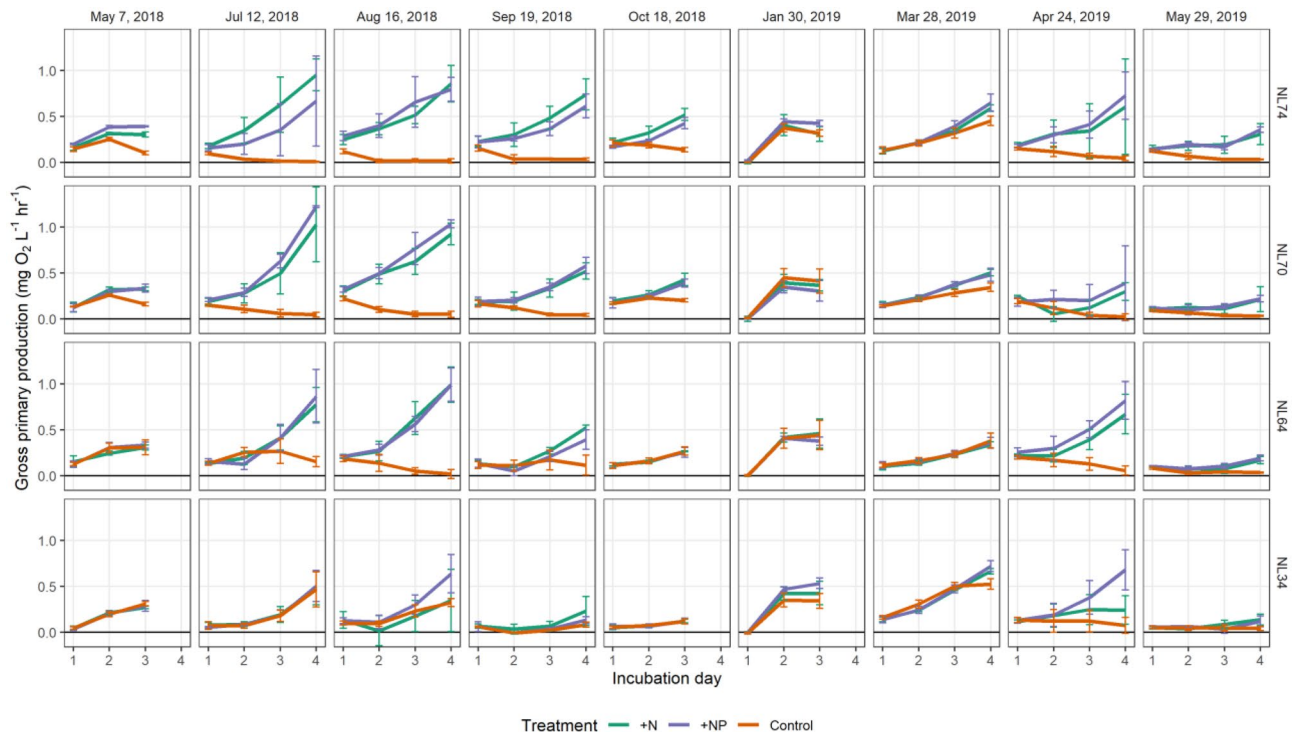
Fig. 2 Laboratory-based rates of gross primary production (GPP) among nutrient treatments. Each panel is a 3–4-day incubation. Water was collected at four sites (rows) on nine dates (columns). The seaward site (NL34; bottom row) did not show signs of nitrogen (N) limitation as the control (brown) and nutrient-amended (green and purple) incubations had similar rates. Moving landward (up), the potential for N limitation increased shown as a divergence between the control and nutrient-amended treatments. Maximum N limitation potential occurred in the landward sites during the mid to late summer (Jul–Sept). Error bars show the standard deviation among replicates

sampling campaigns occurred every other week. We also sampled less frequently (2 times per week) during spring tides to monitor longer timescale responses and to discern if the system returned to pre-fertilization conditions. In total, we sampled on 27 dates between July 8 and Aug 26, 2019. Discrete and continuous data are available at Lenoch et al. (2021b) and U. S. Geological Survey (2020).

Sampling Methods

We established seven evenly spaced sites (~ 1.2 km apart) between two long-term sampling sites NL70 and NL76 (Fig. 1). The mean (± standard deviation) tidal excursion length at the central site was 2.17 km (±0.66), and complete longitudinal mixing over this spatial scale typically occurred on the order of 8.4 h (Lenoch et al. 2021a). Thus, our sampling sites were longitudinally mixed within our study area. For some analyses, we combined data from all sites to evaluate temporal changes, treating the entire reach as a single manipulated segment.

On each date, we visited each site in the morning (09:00 to 12:00 Pacific daylight time (PDT)) and collected a variety of sensor-based data and water samples to be processed in the laboratory. We characterized depth profiles at 1-m vertical intervals for temperature, SPC, DO, pH, turbidity, and Chl *a* fluorescence using a YSI EXO2 (Xylem, White Plains, NY). We characterized attenuation of PAR within the water column using a LiCor 1400 light meter (LI-1500 Light Sensor, LI-COR Bioscience, Lincoln, NE) with measurements made every 0.25 m through the 2-m photic zone. At each site, we collected discrete water samples for chemical and biological analyses. Water chemistry samples were processed at the University of California-Davis or shipped to commercial laboratories following established protocols (Forster 1995; Eaton et al. 1998; Doane and Horwáth 2003; Nelson et al. 2011). See supplementary material for detailed water sampling and laboratory procedures.

At the beginning and ending of each sample event, we mapped surface longitudinal conditions at a depth of 0.2 m throughout the entire experimental reach. We used a flow-through sampling system that included a water pump, tubing, and flow regulators to route surface water to a Sea-Bird SUNA V2 (Sea-Bird Scientific, Bellevue, WA) and YSI EXO2 equipped with manufacturer supplied flow cells. Sensor data were captured every second (equivalent to ~ 14 m spatial resolution) on a Campbell data logger (Campbell Scientific, Logan,

UT) and georeferenced with a Garmin GPS (Garmin International, Inc., Olathe, KS) to produce maps of surface water chemistry (Crawford et al. 2015; Downing et al. 2016). We mapped the channel by motorboating at ~50 km h^{-1} near the center of the channel. The morning transects (~08:00 PDT) began at the top of the DWSC (near the boat ramp and the locks) and proceeded seaward, ending at NL70 (13 km). The afternoon transects (~12:00 PDT) proceeded in the opposite direction. All transects lasted ~20 min. Point data were snapped to a line running through the middle of the channel, allowing us to linear reference all observations, calculate dispersion (Lenoch et al. 2021a), and evaluate how spatial gradients (e.g., fertilizer plug) evolved through time. Sensor data from the flow-through system were also linked with each discrete sample collected at the seven sampling sites after allowing the system to stabilize for at least 2 min.

Instrument Moorings

A network of stationary, floating sensor arrays (Fig. 1) was deployed to continually monitor physical, chemical, and biological conditions. All sensors were attached to floating buoys, allowing them to maintain their vertical position relative to the water surface. We deployed two types of arrays, one in the littoral zone and one farther offshore. The littoral array was located at station NL74, ~20 m offshore in 1–4 m depth to prevent loss of equipment due to ship traffic and configured to sample every 15 min (USGS station ID 383019121350701). Sampling was done using a YSI EXO2 (measuring temperature, SPC, DO, pH, turbidity, fDOM, and algae fluorescence) and a Satlantic SUNA V2 nitrate sensor, both configured with wipers. A total of 5 offshore arrays were located ~30 m from shore, anchored in 6–8 m water at additional sites (data available in Lenoch et al. 2021b). Each pelagic array included three optical DO loggers (PME minidot) positioned at depths of 1, 2.5, and 4 m, three temperature loggers (Onset Hobo U22s) positioned at depths of 1.5, 3, and 4.5 m, and three conductivity loggers (Onset Hobo U24s) positioned at depths of 0.5, 2, and 3.5 m (Loken et al. 2021). The pelagic arrays allowed monitoring of vertical dynamics of temperature, SPC, and DO, which were used to calculate stratification and metabolism (Lenoch et al. 2021a; Loken et al. 2021).

Some daily metrics were calculated from the continuous sensor arrays. For turbidity and NO_3, we calculated daily means (midnight to midnight). Because Chl *a* had a strong diel signal and occasionally had spuriously high values, the 75th percentile of daily Chl *a* was used to represent each day's Chl *a* condition. From the vertical temperature arrays, we calculated Schmidt stability using the R package rLakeAnalyzer (Winslow et al. 2019). We then summarized Schmidt stability by calculating the daily mean as an indicator of the daily strength of stratification. Daily metrics

were only calculated for days and variables with at least 90% coverage after data quality control.

Phytoplankton Productivity

Daily Chl *a* concentration and integrated rates of GPP and NEP were used to evaluate short timescale changes in production as it related to fertilization and other dynamics. In this analysis, we used the 75th percentile of daily Chl *a* at the central buoy (NL74) and metabolic rates calculated using an oxygen isotope approach that was originally described by Quay et al. (1995) and updated in Bogard et al. (2017). The isotope-based metabolism method used water samples collected on 14 dates (~twice weekly) from all seven sites and is thoroughly described in Loken et al. (2021). We chose the isotope method because it characterized the whole-ecosystem, reach-scale response, and it provided a more reliable estimate compared to the other approaches (Loken et al. 2021).

Drivers of daily GPP and Chl *a* were evaluated using multivariate regression models. For daily GPP, we used a mixed-effects model using the lmer function in the lme4 R package (Bates et al. 2015) that included site as a random effect and three predictors as fixed effects (Schmidt stability, NO_3, and turbidity). All fixed-effect predictors were scaled (subtracting the mean from each value and dividing by the standard deviation), allowing direct comparison of the effect magnitude among predictors. For the GPP model, we first tested if a random intercept was justified by comparing Akaike information criterion (AIC) values among models with and without the random effect structure. We then built a global model that included all three fixed effects with interactions and included site as a random effect. To visualize the marginal effect of each predictor (e.g., turbidity) on GPP, we built a similar mixed-effects model but excluded that predictor. The model residuals were plotted against the excluded predictor to show its marginal relation with GPP after accounting for the other fixed and random effects. We performed a similar modeling exercise for daily Chl *a*, but these models only included fixed effects as these data were only collected at the central site (NL74). We used a general linear model in the R stats package using the same three predictors as fixed effects (Schmidt stability, NO_3, and turbidity). Similarly, all predictors were scaled prior to modeling, all interaction terms were included in the model, and the marginal effects of each predictor were visualized by plotting against the residuals of the model lacking the specific predictor.

Timescales

We compared ambient DIN concentrations with metabolic N demand and NO_3 dispersive flux to gain insight into the roles of biology and hydrodynamics in shaping N dynamics.

Accompanying each metabolism estimate, we estimated the amount of N necessary to meet metabolic demand. Rates of GPP and ER were converted to N units based on stoichiometry and growth efficiency following methods outlined in Hall and Tank (2003). This approach requires parameterizing the heterotrophic growth efficiency (HGE) and the carbon:nitrogen molar ratio (C:N) of heterotrophs and autotrophs. Rather than using fixed model coefficients, N demand was calculated using two HGEs (0.05 and 0.2) and two C:N ratios (6 and 12). We used multiple coefficients to bound the estimates of N demand under a variety of plausible system-specific C:N (Cloern et al. 2002; Young et al. 2020) and under low and moderate growth efficiency. N demand using the four combinations of coefficients was calculated for each isotope-based metabolism estimate.

The dispersive flux of NO_3 was calculated at the central site (NL74) using continuous NO_3 concentrations (*C*) and discharge (*Q*) based on a side-looking acoustic Doppler deployed at NL74. Instantaneous flux of NO_3 (lacking high frequency measurements of NH_4 we were unable to compute dispersive flux of DIN) was separated into advective and dispersive components using the following equation (Geyer et al. 2001):

$$Total\ flux = advective\ flux + dispersive\ flux$$

$$<Q \cdot C> = <Q> \times <C> + <Q'> \times <C'>$$

where $<\ >$ indicates the tidally averaged value, and $'$ indicates deviations of the instantaneous (15 min) measurement from the tidally averaged value. The flux decomposition allows the NO_3 flux to be separated into components due to net flow (advective) and tidal dispersion (dispersive). Instantaneous dispersive flux estimates were converted to daily rates and averaged during the non-fertilization period (Aug 15 to Sept 15) to approximate the amount of N transported landward during baseline conditions across a range of tidal conditions (one spring-neap cycle). This approach assumes concentrations are vertically homogenous and thus does not account for vertical gradients in longitudinal flux stemming from benthic N efflux, stratification, and uptake in the photic zone. We scaled dispersive flux estimates by dividing the average load during the non-fertilized period by the volume of the average excursion length (2.17 km) over the study reach, which, given the assumptions involved, provides only a first-order approximation (see supplementary material for more detail). Demand was based on modeled metabolic rates and several coefficients that were not calibrated, likewise providing only a first-order approximation of fluxes. We use these rate estimates along with ambient concentrations to gain insight into the relative magnitudes of the N pool, use, and delivery.

Algae doubling rates were also used to evaluate phytoplankton growth dynamics. We calculated the average Chl *a* production rate by converting the average volumetric rate of GPP to Chl *a* units using a photosynthetic quotient of 1, the average carbon to Chl *a* ratio (41:1) from Jakobsen and Markager (2016), and assuming half of GPP goes toward biomass. We then scaled the Chl *a* production rate by the average Chl *a* plus pheophytin concentration measured in the lab to estimate the algal doubling rate. We performed a similar calculation but scaled the volumetric rate to the photic zone to simulate phytoplankton growth in a stratified water column. Together with the N rate estimates, the time-scales of phytoplankton growth provide insight into coupled physical-biogeochemical dynamics (Lucas and Deleersnijder 2020).

Results

Evidence Suggesting Nutrient Limitation

Long-term monitoring and laboratory incubations identified spatial and temporal variability in the potential for N to limit production (Figs. 2 and S3). In the DWSC, NO_3 comprised on average 72% of the DIN; thus, patterns of NO_3 provide a reasonable view of DIN across the study. However, NH_4 makes up a larger proportion of DIN when and where NO_3 concentrations are lowest. DIN (and NO_3) concentrations were lowest in the upper DWSC, decreasing through the spring (Mar–May) and remaining low through Sept. Collectively, the long-term DIN patterns support the potential for N limitation to be strongest in the upper DWSC during the late summer.

Laboratory incubations confirmed similar spatial and temporal patterns in N limitation potential. During the late fall through early spring (Oct–Mar), there were minimal differences in GPP between the control and the nutrient-amended incubations (Fig. 2), suggesting neither N nor P increased primary production during these periods. In contrast, GPP in the +N and +NP incubations diverged from the control group in Apr and the summer months (July–Sep), and this divergence varied spatially (Fig. 2). The farthest landward site (NL74) tended to have larger differences between the control and nutrient-amended groups, which started earlier in the year and earlier in the incubation. At this site, GPP in the control treatment was near zero on days 2–4 of the incubation during the summer, while GPP in the nutrient-amended treatments increased progressively each day upwards of 0.9 mg O_2 L^{-1} h^{-1}.

Response to Experimental Addition of Nitrogen

In total, we applied 10,886 kg of calcium nitrate (1687 kg of NO_3-N) to the DWSC using a crop-dusting airplane. Following each of eight applications of 211 kg of NO_3-N, NO_3
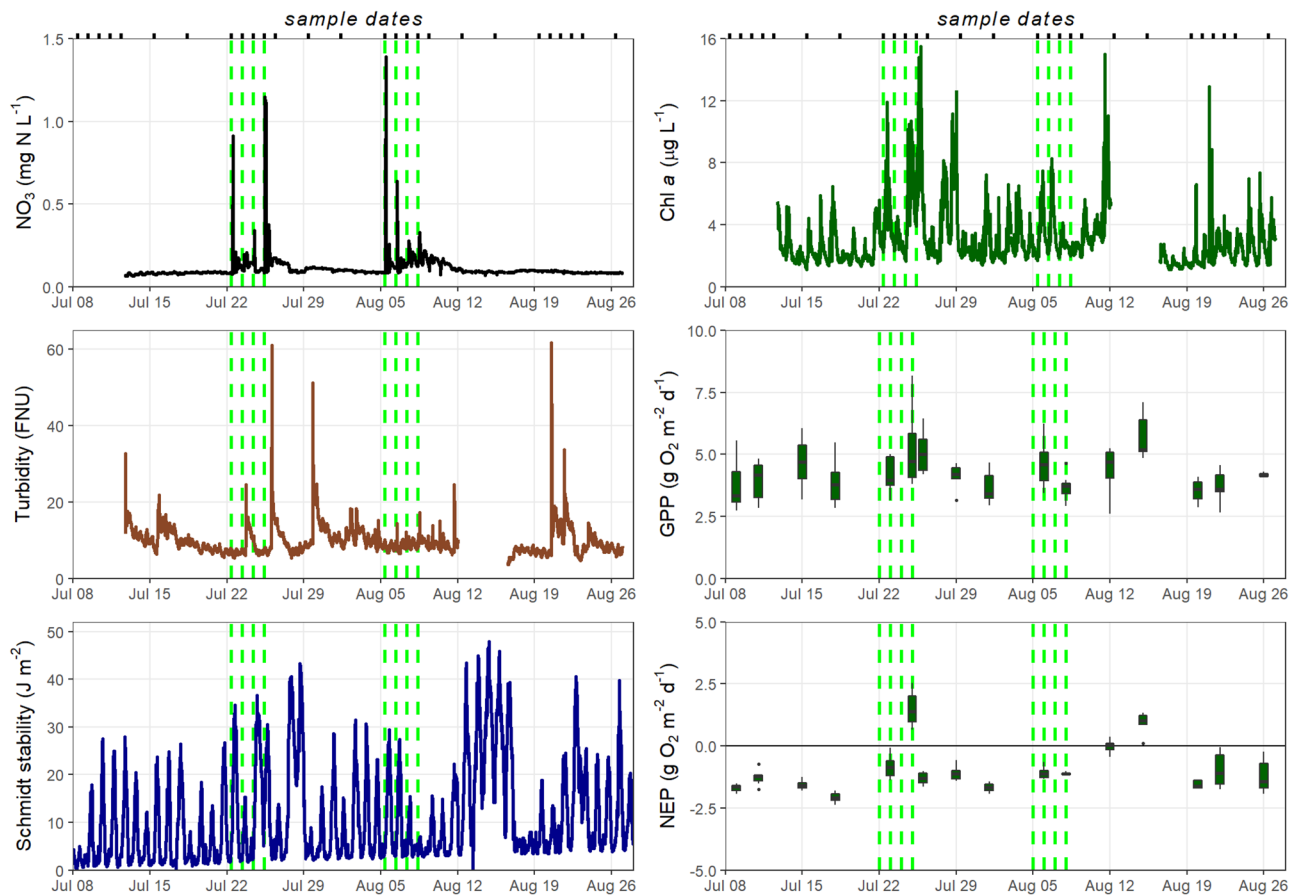
Fig. 3 Time series of potential drivers of production (left; nitrate (NO₃), turbidity, and Schmidt stability (i.e., stratification strength)) and production response variables (right; chlorophyll a (Chl *a*), gross primary production (GPP) and net ecosystem production (NEP)). Ver-

tical dashed green lines note when calcium nitrate was applied. Missing data for Chl *a* and turbidity resulted from sensor failure. GPP and NEP show the daily distribution among sites for days with isotope-based metabolism estimates (see Loken et al. 2021)

concentrations increased in the application area (Fig. 3). The fertilizer typically dissolved within the upper 3 m of the water column and subsequently mixed with the deeper water column. NO_3 concentrations at the central site (~ 1 m depth) increased between 0.1 and 1.2 mg N L^{-1} on fertilization days. Some applications caused immediate and sharp increases in NO_3 as the fertilizer plug remained intact while it advected past the stationary sensor. Following other applications, the fertilizer plug dispersed quickly (Fig. 3). In the morning following each fertilization, concentrations through the entire reach did not exceed 0.16 mg N L^{-1}, and concentrations returned to background levels within 3–5 days of application.
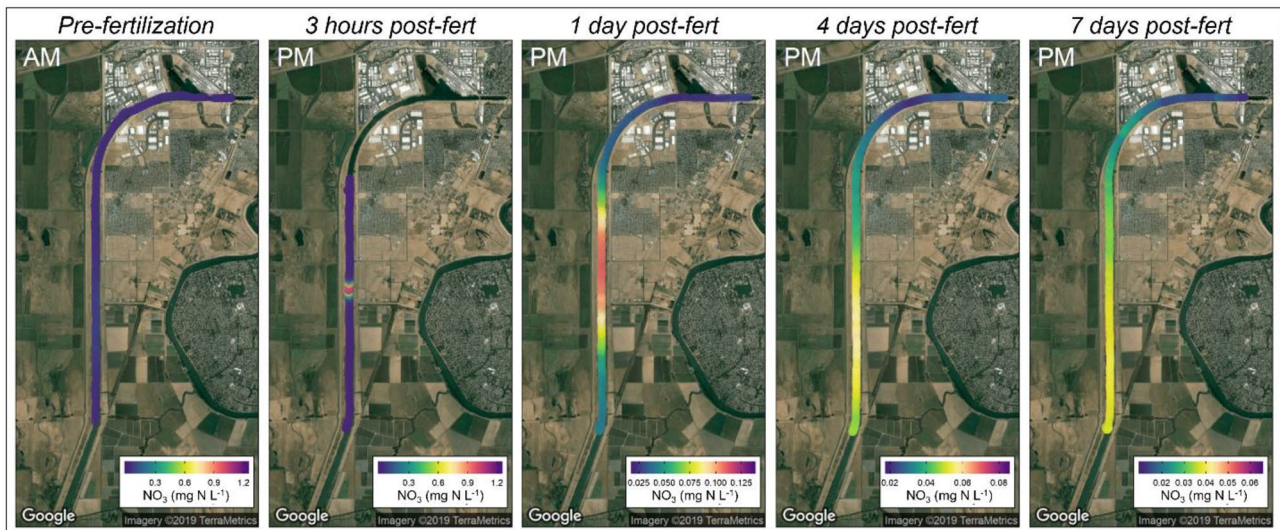
Spatial patterns of NO_3 following fertilizations were consistent with dispersion and mixing timescale estimates, which varied spatiotemporally with tidal currents and wind (Lenoch et al. 2021a). For example, immediately following the final application of the first fertilization week (July 25), NO_3 exceeded 1.2 mg N L^{-1} in a small geographic area (~ 500 m in length; Fig. 4). On the following morning, NO_3 concentrations throughout the entire reach were below 0.15 mg N

L^{-1}, and the fertilized plug had grown to ~ 4 km in length (Fig. 4). Four days after fertilization, the maximum concentration decreased to 0.06 mg N L^{-1}, and the fertilized plug had expanded in length beyond the sampling extent (Fig. 4). Seven days following fertilization, the fertilized plug was no longer detectable and the spatial pattern of NO_3 returned to its typical longitudinal gradient (Fig. S1). Based on dispersion estimates, the timescale for complete longitudinal mixing (within a 2.1-km tidal excursion) would be ~ 8 h, and we would therefore estimate ~ 20 h after fertilization that the extent of the NO_3 would be about ~ 5 km in length. Moreover, we would expect NO_3 to be dispersed along an extent of ~ 40 km in 7 days, and therefore concentrations of NO_3 to be an order of magnitude lower than the concentration after 1 day.

Variation in Factors Regulating Light Availability to Phytoplankton

Turbidity at the central site (NL74) varied between 4.3 and 61.8 FNU over the 2-month record. Higher turbidities occurred

Fig. 4 Spatial pattern of nitrate (NO_3) prior to and following fertilization. On July 23, 2019 (left two panels), calcium nitrate was applied to a 400-m segment. The fertilized plug gradually expanded and decreased in concentration. In this example, the elevated NO_3 levels completely eroded sometime between 4 and 7 days after fertilization. The first two panels share a color ramp, while the color ramp in the other three is based on daily minimum and maximum nitrate concentrations

at slack after floodtides (high tides) through advection of the longitudinal gradient in turbidity (Figs. 3 and S5). Overlaid on this sub-daily tidal signal, there were several dramatic spikes in turbidity, increasing upwards of 10 times background levels and remaining elevated for up to 3 days. These turbidity spikes aligned with the passage of large cargo ships through the DWSC. Overall, we witnessed 21 ship passes (captured on a time lapse camera between July 15 and Sept 14). In general, regular ship traffic caused pronounced increases in turbidity, which reduced water clarity for a couple of days.

Water temperature and stratification also varied temporally. Overall, surface temperature at the central site (NL74) ranged between 23.7 and 28.1 °C, and daily ranges varied between 0.6 and 3.5 °C. On most days (64 out of 78), the water column stratified (Lenoch et al. 2021a) as noted by increases in Schmidt stability (> 5 J m^{-2}; Fig. 3). Schmidt stability ranged between 0.1 and 47.9 J m^{-2} and generally returned to near zero on most days, indicating the breakdown of stratification each evening. There were 5 days total (e.g., July 27–28 and Aug 13–16) when Schmidt stability exceeded 40 J m^{-2} during the day and remained elevated (> 10 J m^{-2}) overnight, indicating strong daytime stratification that persisted overnight. On 18% of days (14 of 78), stratification did not develop, which generally occurred on windy days (Lenoch et al. 2021a).

## Phytoplankton Response: Chlorophyll *a* and Gross Primary Production

Despite successfully raising NO_3 concentrations in our study reach for five continuous days, Chl *a* concentration,

GPP, and phytoplankton biovolume did not increase dramatically (Figs. 3 and S6). Over the 2-month study, the Chl *a* concentration time series at the surface ranged between 1.1 and 15.5 µg L^{-1} and remained in a similar range of variability during both fertilization and non-fertilization periods. Consistent diel signals were detected with maximum values typically occurring in the afternoon, especially on days with pronounced stratification. On average, Chl *a* increased 5.7 µg L^{-1} from the overnight low to the afternoon peak, and the daily increase in Chl *a* ranged between 1.3 and 14.7 µg L^{-1}.

Daily Chl *a* concentration had univariate relations with NO_3, turbidity, and stratification strength (Fig. 5). Daily Chl *a* concentration was positively correlated with NO_3 ($p = 0.004$, $R^2 = 0.17$) and negatively correlated with turbidity ($p = 0.07$, $R^2 = 0.06$). However, stratification strength also correlated with Chl *a* and explained a greater proportion of the variability ($p < 0.001$, $R^2 = 0.51$). The multivariate model indicated that stratification strength and NO_3 were positively related to Chl *a* (Fig. 5; Table 1; *p*-values < 0.001). The marginal effect of turbidity on Chl *a* was not significant ($p = 0.48$; Table 1). Furthermore, there was a significant positive interaction ($p = 0.002$) between stratification strength and NO_3. Aligning with this positive interaction term, Chl *a* concentration near the surface was highest on strongly stratified, fertilized days (Figs. 3 and S7).

Similar to Chl *a*, GPP did not respond dramatically to fertilization. GPP ranged between 2.6 and 8.2 g O$_2$ m^{-2} d^{-1}, with a grand mean of 4.3 g O$_2$ m^{-2} d^{-1}. ER and NEP also did not vary in response to fertilization (Loken et al. 2021). Stratification and light appear to have the biggest effect on
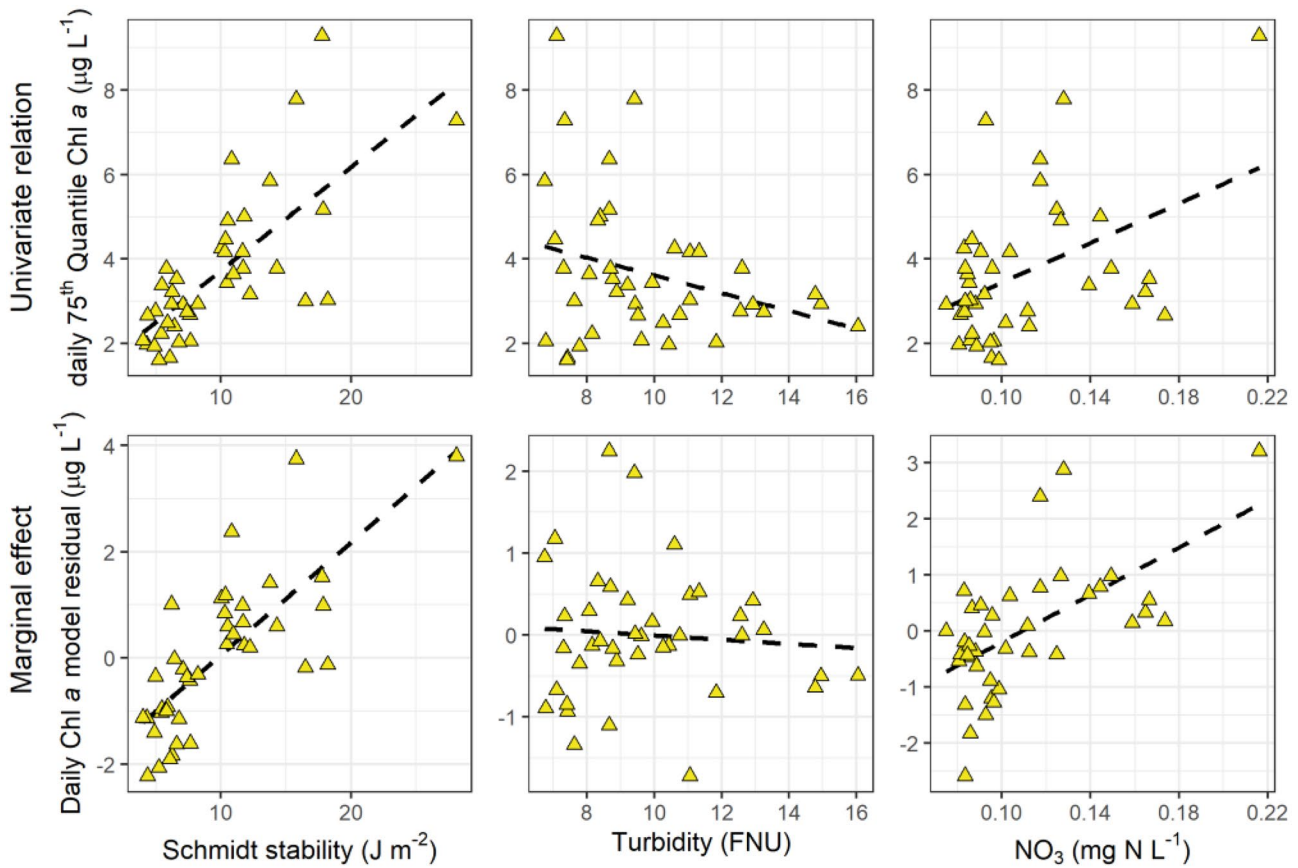
Fig. 5 Drivers (*x*-axis) of daily chlorophyll *a* (Chl *a*) concentrations at the central site (NL74). The top row is the univariate relation between each driver and the daily 75th percentile Chl *a* concentration. The lower 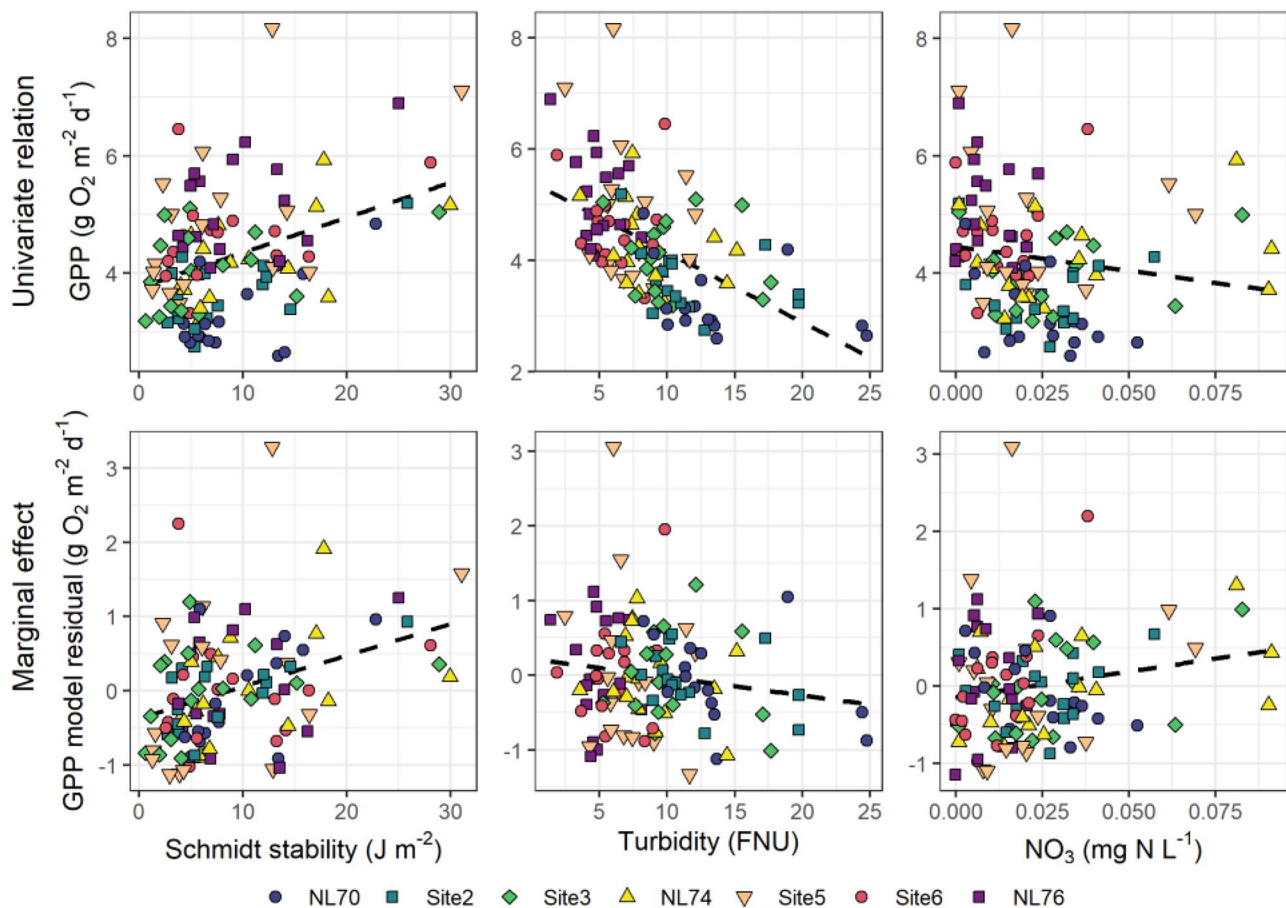row is the marginal effect of each predictor variable, where the *y*-axis is the residual from the fixed-effects model that did not include that predictor. *X*-axes are the daily mean Schmidt stability, turbidity, and nitrate (NO_3). Only days with at least 90% temporal coverage are included. Best fit linear regression plotted in each panel

GPP (Fig. 6; Table 2). Daily rates of GPP were positively correlated with Schmidt stability ($p < 0.001$, $R^2 = 0.13$) and negatively correlated with turbidity ($p < 0.001$, $R^2 = 0.28$). GPP had a weaker univariate relationships with NO_3 ($p = 0.10$, $R^2 = 0.02$). The mixed-effects model indicated

that stratification strength had the strongest positive effect on GPP ($p < 0.001$, Fig. 6, Table 2). Nitrate also had a weak but positive effect on GPP ($p = 0.07$), whereas turbidity had a negative effect ($p = 0.04$). There were significant interactions between stratification strength and turbidity together

Table 1 Results of linear fixed-effects regression for chlorophyll *a* at site NL74. Fixed effects were scaled prior to modeling, so the estimates can be compared

	Estimate	Confidence interval	p-value
Fixed effects			
(Intercept)	3.82	3.50–4.14	< 0.001
Schmidt stability	1.38	0.99–1.77	< 0.001
Nitrate	1.11	0.63–1.59	< 0.001
Turbidity	0.12	−0.21–0.46	0.476
Nitrate * Schmidt stability	0.96	0.37–1.56	0.002
Nitrate * turbidity	0.24	−0.21–0.70	0.290
Schmidt * turbidity	0.13	−0.29–0.56	0.537
Nitrate* Schmidt stability * turbidity	0.70	0.11–1.29	0.020
Global model summary			
Number of observations (days)	40		
Conditional R^2	0.79		

Fig. 6 Drivers (*x*-axis) of daily gross primary production (GPP). The top row is the univariate relation between each driver and GPP. The lower row is the marginal effect of each predictor variable, where the *y*-axis is the residual from the mixed-effects model that did not include that predictor. *X*-axes are the daily mean Schmidt stability and discrete measurements of turbidity, and nitrate (NO_3). Points colored by site. Best fit linear regression plotted in each panel

and between all three predictors. The mixed-effect model's conditional R^2 (0.58) was more than double the marginal R^2 (0.24), indicating that the random effects (i.e., site) explained more of the total variation in GPP than the fixed effects. Thus, one or more factors varying spatially play an important role in shaping GPP within this reach.

Scaling the average volumetric rate of GPP (0.53 mg O_2 L^{-1} d^{-1}) to Chl *a* units, the estimated average Chl *a* production rate was 2.42 µg Chl *a* L^{-1} d^{-1}. This calculation does not consider loss pathways, but it does match the typical daytime increase in Chl *a* during non-stratified days (Fig. 3). Scaling this production rate to the average Chl *a* plus pheophytin concentration (6.6 µg L^{-1}) suggests an algal doubling rate of 2.7 days. Chl *a* production could also be scaled only to the photic zone (2.7 m), which would imply a growth rate of 7.13 µg Chl *a* L^{-1} d^{-1} and a doubling rate of 0.9 day. The growth rate is faster if the water column is stratified, and the magnitude aligns with the Chl *a* time series during strong stratification (Fig. 3).

Spatial Patterns

Multiple physical, chemical, and biological properties of the DWSC were organized longitudinally (Figs. 7 and S1). As expected (Feyrer et al. 2017), turbidity was highest at the most seaward site (NL70) and gradually declined moving landward. Consequently, light attenuation coefficients decreased and Secchi depth increased moving landward, reflecting greater water clarity in the upper channel. DIN, NO_3, and NH_4 also declined moving farther landward. After excluding days with or following fertilization, mean concentrations of DIN at the lowest and uppermost station were 0.05 and 0.02 mg N L^{-1}, respectively. Concentrations of NO_3 and NH_4 were of similar magnitudes; the farthest seaward station had average concentrations of 0.02 mg NO_3-N L^{-1} and 0.03 mg NH_4-N L^{-1}, whereas the farthest landward station had average concentrations of 0.01 mg NO_3-N L^{-1} and < 0.01 mg NH_4-N L^{-1}.

Table 2 Results of linear mixed-effects regression for gross primary production. Sites were included as random effects. Fixed effects were scaled prior to modeling, so the estimates can be compared

	Estimate	Confidence interval	p-value
Fixed effects			
(Intercept)	4.28	3.81–4.76	< 0.001
Schmidt stability	0.44	0.25–0.62	< 0.001
Turbidity	−0.20	−0.39 to −0.01	0.038
Nitrate	0.16	−0.02 to 0.33	0.074
Turbidity * Schmidt stability	−0.36	−0.58 to −0.13	0.002
Nitrate * Schmidt stability	0.02	−0.15 to 0.20	0.779
Nitrate * turbidity	−0.12	−0.34 to 0.10	0.273
Nitrate * Schmidt stability * turbidity	−0.26	−0.48 to −0.05	0.018
Random effects (sites)			
Residual variance	0.45		
Random effects variance	0.36		
Interclass correlation coefficient	0.45		
Number of sites	7		
Site-specific intercepts (i.e., random effects)			
NL70	−0.80		
Site2	−0.50		
Site3	−0.10		
NL74	−0.27		
Site5	0.59		
Site6	0.31		
NL76	0.76		
Global model summary			
Number of observations (site days)	112		
Marginal R^2	0.24		
Conditional R^2	0.58		

Aligning with the spatial pattern in water clarity, integrated water column rates of GPP, ER, and metabolic N demand were also greater in the landward sites (Fig. 7). Mean GPP and ER were 5.16 and −5.91 g O_2 m^{-2} d^{-1}, respectively, at the farthest landward site (NL76), while rates were 3.30 and −4.56 g O_2 m^{-2} d^{-1} at the farthest seaward site (NL70). The mean metabolic N demand among days and model parameters at NL70 was 0.019 mg N L^{-1} d^{-1} and at NL76 was 0.027 mg N L^{-1} d^{-1}. Among model parameters and metabolism calculations, the metabolic N demand ranged between 0.008 and 0.030 mg N L^{-1} d^{-1}, which does not account for dissimilatory processes. In contrast to metabolism and N demand, Chl a concentrations did not vary among the seven experimental sites (Fig. 7). However, Chl a differed spatially at a broader scale (Fig. S1). Maximum Chl a during June through September typically occurs within the experimental reach (i.e., between NL70 and NL76).

Between Aug 15 and Sept 10, 2019, a first-order approximation of the average dispersive NO$_3$ flux was −31.4 mg NO$_3$-N s^{-1}. The flux was negative (landward direction), consistent with the expectation that tidal dispersion would mix out the NO$_3$ spatial gradient. Dividing the dispersive flux (i.e., the load) by the volume of a tidal excursion length (∼ 2.0 × 10^9 L) would imply an increase of 0.001 mg NO$_3$-N L^{-1} d^{-1}, to the reach 2.17 km landward of NL74. This approximation is based on an oversimplistic view of hydrodynamics and does not account for vertical variation in NO$_3$ concentration nor does it include the subsequent landward transport from this reach (see supplementary material). However, these rates approximate the dispersive supply of N that is available to fuel metabolism and other N transformations. Comparatively, the estimated dispersive flux rate is an order of magnitude smaller than the daily N demand and DIN concentration (Fig. 7). Collectively the observed DIN concentrations and the estimated rates of metabolic N demand and dispersive flux suggest that the whole system should gradually decrease in N over time, consistent with seasonal observations (Fig. S3).

Discussion

Rates of primary production in estuaries can vary as much in time as they can in space, both within and across systems (Cloern et al. 2014), underscoring the need to understand the mechanisms driving such variations. In a large terminal

Fig. 7 Spatial patterns of turbidity, gross primary production (GPP), chlorophyll a (Chl *a*), ecosystem respiration (ER), dissolved inorganic nitrogen (DIN) concentrations, and metabolic nitrogen (N) demand. The two N panels (bottom row) share a comparable logged *y*-axis, allowing direct comparison of standing stock, daily demand, and daily dispersive flux. Landward dispersive nitrate (NO$_3$) flux plotted as a dotted line. Each box is the distribution through time at each experimental site arranged from seaward (NL70) to landward (NL76). The upper and lower edges are the 25th and 75th percentiles, whiskers are drawn up to 1.5 times the interquartile range, and points are plotted if beyond the whiskers. Declining turbidity allows increases in GPP and ER and elevated N demand despite similar Chl *a* concentrations. DIN concentrations are near the metabolic N demand at the landward stations
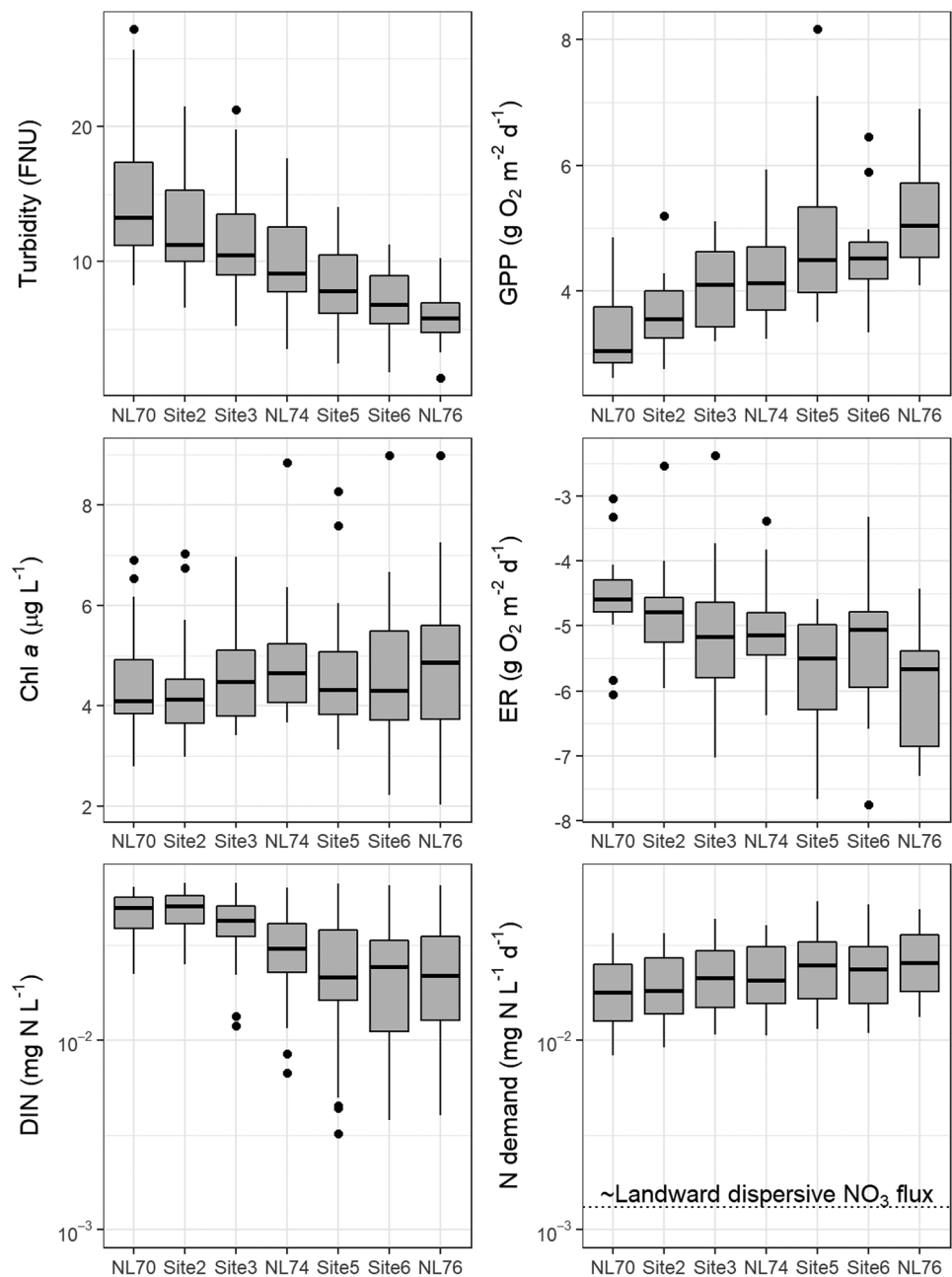
slough, interactions among hydrodynamics, light, and nutrients collectively regulate phytoplankton and metabolism dynamics. Production did not respond strongly nor consistently to NO$_3$ fertilization, suggesting that N was likely not its sole driver. Although our whole-ecosystem experimental N additions aimed to elevate and maintain NO$_3$ within a confined volume, tidal dispersion eroded the spatial gradient in NO$_3$ in a matter of hours, with concentrations returning to background within a few days, thereby preventing a prolonged ecosystem response. Tidal dispersive mixing also served to continually transport NO$_3$ landward from the turbidity maximum zone located seaward of our experimental

reach (Fig. 7). Temporal and spatial patterns of Chl *a* and GPP were most strongly related to stratification, highlighting the role hydrodynamics play in regulating production in this system. However, Chl *a* was also positively related to NO$_3$, which had a positive interaction with stratification strength, suggesting stratification may trigger N limitation. While continual NO$_3$ dispersive mixing and ambient DIN concentrations may have been sufficient to sustain metabolic demand of the existing phytoplankton biomass during the experiment, nutrient enrichment incubations suggest phytoplankton isolated within the photic zone during periods of prolonged stratification likely became N limited over the course of the day.

Extrapolating our results to the entire DWSC, productivity appears to transition from a light-limited to a nutrient-limited state moving farther landward in the channel, with the potential for maximum phytoplankton productivity to occur near the transition between these conditions. The emergence and specific location of this transition as well as its magnitude will vary in accordance with hydrodynamics, seasonality, and short-term disturbances, such as ship traffic and heat waves. In this context, dispersion serves to redistribute nutrients to areas where production may be limited and phytoplankton to areas where it can subsidize the food web (Cloern 2007). All told, our experiment highlights the complexities in strong tidally forced systems, their inherent temporal and spatial variability, and the need to account for hydrodynamics, habitat heterogeneity, and connectivity to evaluate biogeochemical processes with complex source-sink dynamics. Our results emphasize the need for coupled hydrodynamic-biogeochemical-phytoplankton growth models for effectively understanding such dynamics.

Ecosystem Response to Experimental Nitrogen Addition

Dispersion and stratification mediated the effect of NO_3 additions on productivity. Together the NO_3 time series at a fixed location and the spatial patterns of NO_3 through time illustrate the temporal and spatial scales of the experimental manipulation. The entire 7-km reach typically mixes on the order of 1–2 days (Lenoch et al. 2021a), and all sampling locations showed significant tidal timescale variability in the variables measured in this reach. Because NO_3 concentrations returned to background within 3–5 days, the two fertilization weeks appear to have been spaced sufficiently far apart to allow the system to return to background prior to the second round of fertilizer application (Fig. 3a). We cannot account for carry over effects that may have persisted as communities of bacteria, phytoplankton, and zooplankton responded to manipulation, but plankton abundances did not change discernibly in response to fertilization (Fig. S6). Given the fast dispersal and limited effects, we proceed cautiously under the assumption that the two fertilization weeks were independent.

Productivity did not respond consistently following NO_3 additions, primarily due to tidally driven dispersive mixing, stratification, and light limitation. Daily Chl a at the center of the fertilizer addition had the strongest correlation with stratification strength (Table 1). While surface water temperature also co-varied with Chl a, we suspect the increase in productivity to be primarily driven by vertical isolation. The greater increase in Chl a on warmer, stratified days and the corresponding increase in phytoplankton growth rate were much larger than would be expected from the relationship between phytoplankton growth rate and temperature

alone (Boyd et al. 2013; Kremer et al. 2017). Furthermore, the absolute range in water temperatures was 23.7–27.8 °C, which is near the temperature optima for many phytoplankton species at this latitude (Boyd et al. 2013). Thus, we suspect the elevated Chl a with warmer waters to be the result of stratification, allowing phytoplankton to congregate and (or) proliferate in the photic zone and signaling the importance of vertical mixing on controlling temporal phytoplankton dynamics. While stratification in estuaries is often regulated by tidal currents, wind can be an important factor controlling vertical mixing dynamics in the upper DWSC (Lenoch et al. 2021a) and other open estuarine areas (Yin et al. 1997; Lucas et al. 2006; Jones et al. 2008). In the upper DWSC during the summer months, wind-driven shear was needed to overcome temperature-driven buoyancy (Lenoch et al. 2021a), which is evident during periods of persistent stratification through complete tide cycles, which suggests that mixing by tidal currents alone cannot overcome the buoyancy (Fig. 3).

Spatial and temporal patterns of GPP were related to turbidity and stratification strength, both of which are tightly linked to hydrodynamics. Based on the mixed-effects model, stratification was the strongest driver of GPP (Table 2). Because the model included site as a random effect, the fixed effects primarily explain temporal variation. The strongest univariate driver of daily GPP was turbidity (Fig. 6), which varied spatially (Fig. 7), and thus was accounted for as a random effect in the model (Table 2). The spatial pattern in turbidity is controlled by water velocity in two ways: (1) the landward transport of suspended sediment into the study reach (2) local erosion and deposition during the tidal current maxima and slack water, respectively. Spatial and temporal patterns of turbidity and stratification can vary immensely at a range of temporal and spatial scales, which likely contribute to variations in primary production within estuaries.

Coupling hydrodynamics with light attenuation and spatial variability provides a more realistic view of drivers of productivity. Because of the relatively high turbidity, most of the water column is in the aphotic zone. According to critical depth theory, algal blooms can develop when the depth of the surface mixed layer is shallower than the critical depth, as production rates exceed consumption processes (Sverdrup 1953; Platt et al. 1991). Stratification events temporarily isolate the upper mixed layer, allowing phytoplankton to proliferate while isolated in the photic zone and away from benthic grazers (e.g., clams). During days without stratification, Chl a in the photic zone did not increase more than 2 µg L^{-1} (Fig. 3), suggesting that the critical depth may be shallower than the 7.5 m mean depth of the DWSC. The regularity of complete vertical mixing may prevent sustained algal blooms as has been found in another part of the delta that temporarily stratifies (Lucas et al. 1998). Together, the two key drivers of

production—turbidity and stratification strength—mediate phytoplankton access to light.

In the greater Bay-Delta ecosystem, others have estimated the critical depth to be approximately 5 times the photic depth, implying that blooms can develop when 20% of the upper mixed layer is illuminated (Cloern 1987; Kimmerer 2004). Although this theory has been criticized because of its oversimplification (Behrenfeld 2010), it provides context for phytoplankton dynamics in the DWSC. The average light attenuation coefficient at NL74 during our study was 1.8 m^{-1} (Loken et al. 2021), implying an approximate 1% photic depth of 2.7 m and critical depth of 13.5 m (based on Cloern 1987). The actual critical depth is unknown, but according to this model (Cloern 1987), algal blooms are likely at NL74, which may explain why Chl a increased to some extent each day (Fig. 3). However, prolonged algal blooms and elevated Chl a only occurred during stratified periods, signaling that the true critical depth may be shallower. The relative rates of consumptive processes within the DWSC may be larger than the systems in which the model was developed. Elsewhere in the delta, phytoplankton growth rarely exceeds the combined grazing pressure by zooplankton and bivalves (Kimmerer and Thompson 2014). Although clam densities in the DWSC are relatively low compared to other parts of the delta (Shrader et al. 2020; Zierdt Smith et al. 2021), clam grazing may nevertheless exert a substantial loss rate on phytoplankton when the water column is vertically mixed and contribute to the positive effect of stratification on Chl a and GPP. The actual critical depth will vary in accordance with site-specific community dynamics, but the temporary proliferation during stratification aligns with the theory.

Alternatively, the dispersive flux may prevent algae bloom formation. The water in the experimental reach represents a dynamic integration between landward and seaward ecosystems, and typically has the highest Chl a of the entire DWSC during mid to late summer (Fig. S1). Moving seaward, light decreases, and moving landward, nutrients decrease, which may limit productivity in these connected ecosystems (see the "Connectivity, Hydrodynamics, and Timescales" section). Similar to the applied fertilizer (Fig. 4), phytoplankton will disperse away from local maxima, replaced by lower concentrations from neighboring locations. The seaward ecosystem has an even shallower critical depth than our study site due to higher turbidity and is less likely to stratify due to faster velocities, suggesting rates of primary production will be lower. Moving landward, DIN concentrations decrease (Figs. S1 and S3) to a level below our estimate of metabolic N demand (Fig. 7), suggesting N limitation. Thus, continuous dispersive mixing of water along the length of the DWSC blends the pelagic communities and metabolic signals, which ultimately may prevent algal bloom formation. The timescales of dispersive mixing and the integration of processes

along the DWSC mediate local phytoplankton dynamics and ultimately the ecosystem response to fertilization.

Connectivity, Hydrodynamics, and Timescales

Hydrodynamics create longitudinal spatial gradients in water clarity and nutrients in the DWSC, which collectively are proposed as key regulators of production in the greater delta ecosystem (Jassby et al. 2002; Cloern et al. 2014) and in other estuaries (Caffrey 2004; Barbosa et al. 2010; Domingues et al. 2011). The DWSC is a flood-dominant channel defined as having faster velocity floodtides compared to ebb tides (Morgan-King and Schoellhamer 2013; Lenoch et al. 2021a). Floodtide increases in bed shear stress cause net-import of sediments and other suspended material into the DWSC, contributing to the persistence of a turbidity maximum zone (Figs. S1 and S2), as found in this and other estuaries (Friedrichs and Aubrey 1988; Morgan-King and Schoellhamer 2013; Feyrer et al. 2017). Seaward of the turbidity maximum, water is a mixture of the greater delta waterway and is less likely to stratify due to faster currents. Landward of the turbidity maximum, dampening flow velocities and shortening tidal excursion lengths allow imported sediment to gradually settle as it moves farther into the dead-end channel. Predictable changes in light extinction and stratification overlay the longitudinal pattern in turbidity and flow velocity, leading to increased water clarity (Fig. S1) and more frequent stratification in the landward portion of the DWSC (Lenoch et al. 2021a) and other terminal sloughs.

Combining gradients in flow velocity, water age, and water clarity with biogeochemical processes leads to spatial heterogeneity in other reactive solutes (Fig. S1). As water disperses landward through the DWSC and other terminal sloughs, it gradually ages, increasing the timescales for biogeochemical processes (e.g., autotrophic uptake, denitrification) to transform NO_3 and other reactive solutes (Downing et al. 2016). Water age has been linked to DIN loss in the DWSC (Downing et al. 2016) and flow velocity to rates of N uptake in other parts of the delta (Wilkerson et al. 2015). More broadly, N tends to be the primary nutrient limiting pelagic primary production in estuaries (Howarth and Marino 2006; Elser et al. 2007). The consistent pattern of lowest DIN in the landward DWSC may be further magnified by longitudinal changes in water clarity, which promote higher rates of GPP and metabolic N demand (Fig. 7). Soluble reactive phosphorus (SRP) has an opposing spatial trend, as it generally increases landward along the DWSC longitudinal axis (Fig. S1). Concentrations of SRP rarely fall below 0.04 mg P L^{-1} (Fig. S3), and DIN to SRP molar ratios rarely exceed 10 in the summer months, suggesting that N is generally in higher demand than P. As water and N are continually dispersed landward through the DWSC, some fraction of the original N load is lost (e.g., denitrification), while the typical permanent loss pathways for P

(i.e., burial) may be limited due to tide- and ship-driven resuspension. Together these findings support the hypothesis that primary production in the DWSC and other terminal sloughs can be limited by N, and N limitation is strongest at the landward extents of the channels where water exchange is lower and uptake rates higher (Mallin et al. 1999; Wilkerson et al. 2015; Fig. S6).

Rates of nutrient delivery must be considered in tandem with rates of nutrient uptake (Cloern 2007) and phytoplankton biomass in order to evaluate nutrient limitation. Interestingly, moving landward into terminal sloughs, the compression of tidal excursion causes dispersive mixing to decrease following spatial gradients in dissolved solutes. Within estuaries and other hydrodynamically complex water bodies, the exchange among neighboring habitats may be sufficient to meet stoichiometric demands of primary producers, making the hydrodynamics more influential in controlling the rates of ecosystem-scale biogeochemical processes (Cloern 2007; Crosswell et al. 2017). Similar dynamics are likely occurring for other solutes and ecological processes in the landward extents of other dead-end systems, controlled by the specific length scales of the system (Stumpner et al. 2020b) and the relative rates of dispersion and transformation.

Our experiment illustrated the extent to which production at short timescales responds to interactions among dispersive mixing, stratification, nutrients, and water clarity. Our experiment occurred in a region where light appears to be the primary limiting factor. However, N limitation is spatially and temporally common in many types of estuaries (Boynton et al. 1982; Mallin et al. 1999; Caffrey 2004; Yoshiyama and Sharp 2006), and had the experiment occurred farther landward or in a more isolated part of the delta, there may have been more of an immediate stimulatory effect as the amount of available N may have been insufficient to meet metabolic demand. The exact location of these transitions is unknown and likely varies at multiple temporal scales as hydrodynamics, light, temperature, and nutrient concentrations vary.

Persistent stratification may also result in localized nutrient limitation within the water column. Among days with strong stratification, we observed greater concentrations of Chl a in the photic zone during fertilized periods (Fig. S7). N may become limiting over the course of the day in the DWSC photic zone if it were completely isolated. Based on monthly laboratory incubations (Fig. 2), unconstrained metabolic N demand increases from 0.12 to 0.38 mg N L^{-1} d^{-1} over the course of four consecutive days as phytoplankton biomass accumulated (Table S2). Comparing these daily N needs to the ambient DIN concentration at our experimental reach (~ 0.03 mg N L^{-1}) suggests a completely isolated photic zone may become N depleted at the hourly to sub-daily timescale during a strong stratification event, supporting the notion that intermediate connectivity may maximize productivity (Cloern 2007). Some degree of

vertical connectivity may allow benthic-derived N to mix vertically and support primary production at the surface. These complex vertical dynamics coupled to connectivity and resource limitation at short temporal and spatial scales are difficult to discern and may contribute to high spatial and temporal variability in productivity of estuaries.

Conceptually, production along the longitudinal axis of terminal sloughs like the DWSC is controlled by several hydrodynamic and biogeochemical processes (Fig. 8). N transport from the seaward delta progressively dampens in space and through time as N is consumed and the landward dispersive flux decreases. Production, respiration, and dissimilatory processes can use N, and collectively these processes provide the means to produce the NO_3 spatiotemporal pattern (Figs. S3 and S8). While N delivery declines moving farther landward in the channel, water clarity increases. These conditions provide a means for GPP to increase initially moving landward of the turbidity maximum zone. If light were the sole driver, GPP would increase along the entirety of the channel to its landward terminus. However, long-term data suggest that summertime peak Chl a occurs near our study reach (Fig. S1). This subtle difference suggests that eventually GPP declines, but not because of reduced light availability. If true, this suggests that maximum daily GPP during July and August typically occurs somewhere landward of our experimental reach, but below the channel terminus. Similar non-monotonic relations are evident in river-dominated estuaries where the interplay between nutrient and limit limitation can lead to maximum Chl a at intermediate flushing rates (Qin and Shen 2021). We suspect that N limitation initiates in the uppermost DWSC sometime during the spring or early summer and gradually expands seaward. The exact location of the transition from nutrient to light limitation is unknown and likely blurred by dispersive mixing as discussed previously, varies through time, and may change dramatically at short timescales.

Benthic fluxes and vertical variation in dispersion are missing from our conceptual framework of N dynamics in the DWSC. In other parts of greater delta and San Francisco Bay ecosystem, benthic NO_3 fluxes vary in direction and magnitude. Landward sites tend to have NO_3 fluxes into the sediments on the order of 0–1 mg N m^{-2} h^{-1} (Cornwell et al. 2014). Meanwhile, the flux of NH_4 is typically out of the sediments, ranging up to ~ 1.7 mg N m^{-2} h^{-1} (Cornwell et al. 2014), which is a similar range as determined from a compiled dataset of 48 estuary and coastal sites (Boynton and Kemp 2008). While benthic N fluxes in the DWSC are unknown, applying the average DIN sediment efflux (15 mg N m^2 d^{-1}) calculated by Cornwell et al. (2014) to the 7.5 m water column of the DWSC would result in a loading rate of 0.002 mg N L^{-1} d^{-1}, which is ~ 10% of the metabolic demand and twice the dispersive flux. The diffusive flux out of the sediments would elevate DIN concentrations in the deeper waters of the DWSC
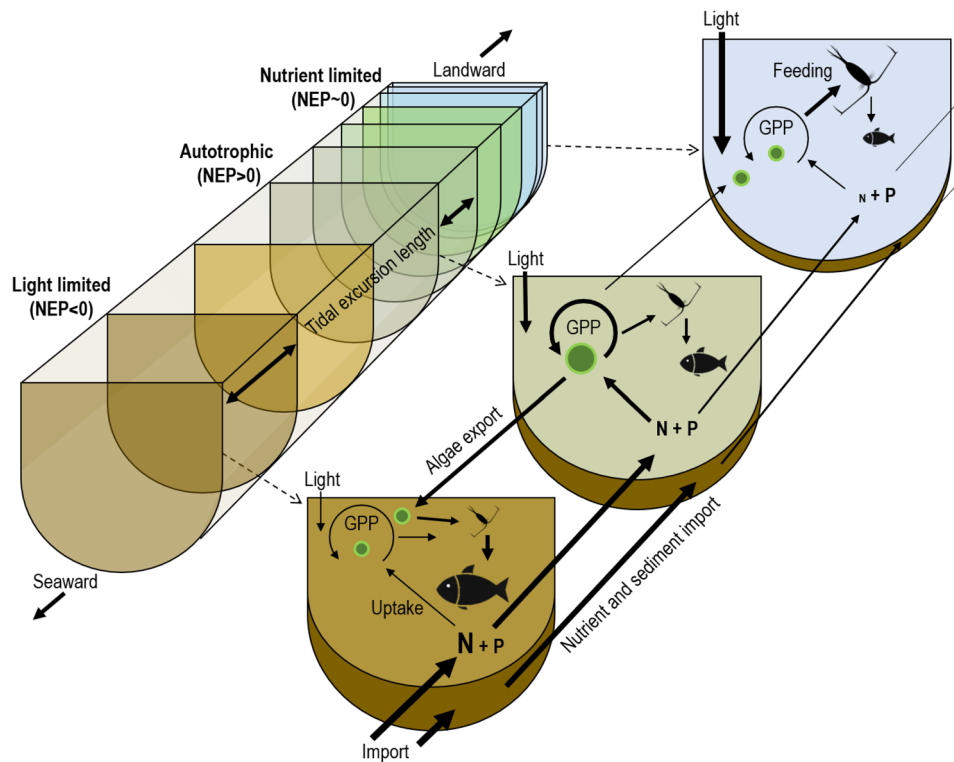
Fig. 8 Conceptual depiction of the major drivers of production in the Sacramento River Deep Water Ship Channel above the turbidity maximum zone. Moving landward, tidal excursion lengths shorten, turbidity decreases, and light availability increases. Sediment and nutrient transport, nitrogen (N) to phosphorus (P) ratios, and N availability also decrease moving farther into the channel. Gross primary production (GPP) in the seaward extent of the channel appears light-limited, while we predict that the landward portion can become N limited. Maximum net ecosystem production (NEP) may occur near the transition from light to nutrient limitation (center inset), which can subsidize landward and seaward food webs. Arrow and icon sizes approximate the relative rates (GPP, transport, uptake) and pool sizes (fish, zooplankton, nutrients), respectively

and may become available to primary producers in the photic zone following vertical mixing. However, benthic-derived DIN may be constrained to the aphotic zone, especially during stratification events, and may be advected longitudinally before mixing vertically. Typically, estimates of benthic flux rates are based on static chamber measurements and do not incorporate flux enhancements associated with water currents and sediment resuspension. Benthic fluxes and sediment resuspension likely increase with tidal velocities and with the passing of large ships. Accurately calculating benthic fluxes in dynamic tidal systems remains a research opportunity, but the recycling of N and other nutrients may be substantial and sufficient to meet the ecosystem need.

Patterns in N availability are in part related to the persistence of the turbidity maximum, which serves as a source of nutrient transport landward and a component of the food web (Feyrer et al. 2017; Young et al. 2020). A large portion of the food web in the lower DWSC (within the turbidity maximum zone) relies on allochthonous and (or) detrital food sources (Young et al. 2020). Low reliance on autochthonous carbon

suggests net heterotrophy in the lower DWSC that may be fueled by the import of organic matter (Fig. 8). The food web of the upper DWSC appears to be supported by a greater amount of autochthonous carbon (Young et al. 2020), suggesting the upper DWSC may be autotrophic and a supply of organic matter and food for higher trophic levels, or a source of such materials for seaward export. Our results indicate a slight spatial gradient in NEP (Loken et al. 2021), aligning with the perception of autotrophic conditions in the upper DWSC (Fig. 8). However, our NEP analysis has a limited temporal and spatial scope. Likely, NEP varies seasonally in accordance with temperature, day length, and nutrients, and we expect a nonlinear spatial pattern in response to variations in hydrodynamics, light, nutrients, and transport (Caffrey 2004; Caffrey et al. 2014; Qin and Shen 2021). Thus, to effectively assess the energetic balance of the DWSC and tidal systems, fluxes and rates need to be assessed at an expanded temporal and spatial scale (i.e., the whole year and along its entire length) and integrated within an ecosystem-wide hydrodynamic framework (Boynton et al. 1982; Crosswell et al. 2017; Wang et al. 2018).

Implications for Management

What are the implications of our study for management actions that may seek to increase production in the greater delta? Although our fertilization experiment did not appear to boost ecosystem productivity, our mechanistic insight into how hydrodynamics, habitat connectivity, and spatial heterogeneity interact to affect rates of whole-ecosystem primary production informs other possibly effective nutrient-based manipulations. First, N additions may have been more effective if applied farther landward where lower rates of dispersive flux, elevated stratification potential, and habitat isolation elevate the potential for nutrient limitation. Using the average metabolic rates at our farthest landward site (NL76; Fig. 7) to represent baseline metabolism of the rest of the landward DWSC, we can approximate the amount of N needed to maintain unconstrained metabolic growth. The total area landward of NL76 is 1.4 km^2 with a mean depth of 6.2 m (Fregoso et al. 2020). Raising NO_3 concentrations by 0.12, 0.17, 0.26, and 0.38 mg N L^{-1} on four consecutive days would meet the demand of unconstrained pelagic primary production based on laboratory incubation (Table S2). If N concentrations were increased throughout the entire water column landward of NL76, it would require ~ 10 times the amount of N applied during our experiment. However, production would be higher in the upper water column, so ideally the N additions could be constrained to the photic zone. If the system were stratified and (or) additions could be maintained in the photic zone, the amount of N needed would be reduced.

Management could also consider algal growth rates and temporary flow diversions in future manipulations. During stratified conditions, the algal doubling rate in the photic zone is on the order of ~ 1 day, suggesting that consecutive nutrient additions to a stratified photic zone have the potential to increase Chl *a* and GPP. Periodic diversion of Sacramento River water, which has both higher DIN concentration and greater water clarity than the DWSC during the summer, through the West Sacramento Lock thus has the potential to both stimulate primary production and export biomass seaward to the turbidity maximum zone and beyond, thereby subsidizing food supply. However, adding net flow would temporarily weaken stratification and may alter the dynamics of the turbidity maximum zone, which in turn could affect other physical, chemical, and biological properties of the DWSC ecosystem.

Conclusions

The DWSC, with its gradients in hydrodynamics, turbidity, and nutrient availability, is a natural laboratory that we used to examine how hydrodynamics and sediment transport mechanisms create spatial heterogeneity that regulates rates of primary production in a terminal slough. Although there is a good conceptual understanding of how light, nutrients, and hydrodynamics together regulate rates of primary production in the delta (Jassby et al. 2002; Cloern et al. 2014), few empirical studies quantify these processes at ecologically relevant spatiotemporal scales. Our experiment demonstrated that persistent and long-term nutrient additions would be necessary to fuel an increase in phytoplankton biomass given the rates of dispersive mixing. The extent to which net production is consumed at a given location by zooplankton and benthic grazers or exported landward or seaward within the system will depend on local population densities and community structure, as well as hydrodynamics via tidal dispersion and the possibility to create net advective flows through gate operations. Thus, quantifying fluxes of carbon and nutrients in a spatially explicit context that includes an understanding of hydrodynamics is critical for determining resource availability for higher trophic levels.

Supplementary Information

Declarations

Competing Interests The authors declare no competing interests.

Disclaimer Any use of trade, product, or firm names is for descriptive purposes only and does not imply endorsement by the U.S. Government.

References

Barbosa, A.B., R.B. Domingues, and H.M. Galvão. 2010. Environmental forcing of phytoplankton in a Mediterranean Estuary (Guadiana Estuary, South-western Iberia): A decadal study of anthropogenic and climatic influences. *Estuaries and Coasts* 33: 324–341. https://doi.org/10.1007/s12237-009-9200-x.

Bates, D., M. Mächler, B. Bolker, and S. Walker. 2015. Fitting linear mixed-effects models using lme4. *Journal of Statistical Software* 67. https://doi.org/10.18637/jss.v067.i01.

Beck, M.W., J.D. Hagy, and M.C. Murrell. 2015. Improving estimates of ecosystem metabolism by reducing effects of tidal advection on dissolved oxygen time series. *Limnology and Oceanography: Methods* 13: 731–745. https://doi.org/10.1002/lom3.10062.

Behrenfeld, M.J. 2010. Abandoning Sverdrup's critical depth hypothesis on phytoplankton blooms. *Ecology* 91: 977–989. https://doi.org/10.1890/09-1207.1.

Bernhard, A.E., and E.R. Peele. 1997. Nitrogen limitation of phytoplankton in a shallow embayment in northern Puget Sound. *Estuaries* 20: 759–769. https://doi.org/10.2307/1352249.

Bernhardt, E.S., J.B. Heffernan, N.B. Grimm, E.H. Stanley, J.W. Harvey, M. Arroita, A.P. Appling, M.J. Cohen, et al. 2018. The metabolic regimes of flowing waters. *Limnology and Oceanography* 63: S99–S118. https://doi.org/10.1002/lno.10726.

Bogard, M.J., D. Vachon, and N. F. St.-Gelais, and P. A. del Giorgio. 2017. Using oxygen stable isotopes to quantify ecosystem metabolism in northern lakes. *Biogeochemistry* 133: 347–364. https://doi.org/10.1007/s10533-017-0338-5.

Boyd, P.W., A.J. Watson, C.S. Law, E.R. Abraham, T. Trull, R. Murdoch, D.C.E. Bakker, A.R. Bowie, et al. 2000. A mesoscale phytoplankton bloom in the polar Southern Ocean stimulated by iron fertilization. *Nature* 407: 695–702. https://doi.org/10.1038/35037500.

Boyd, P.W., T.A. Rynearson, E.A. Armstrong, F. Fu, K. Hayashi, Z. Hu, D.A. Hutchins, R.M. Kudela, et al. 2013. Marine phytoplankton temperature versus growth responses from polar to tropical waters – outcome of a scientific community-wide study. *PLOS ONE* 8: e63091. https://doi.org/10.1371/journal.pone.0063091.

Boynton, W.R., and M.W. Kemp. 2008. Estuaries. In *Nitrogen in the Marine Environment*, 809–866. New York: Academic Press.

Boynton, W.R., M.W. Kemp, and C.W. Keefe. 1982. A comparative analysis of nutrients and other factors influencing estuarine phytoplankton production. In *Estuarine Comparisons*, 69–90. Elsevier. https://doi.org/10.1016/B978-0-12-404070-0.50011-9.

Caffrey, J.M. 2004. Factors controlling net ecosystem metabolism in U.S. estuaries. *Estuaries* 27: 90–101. https://doi.org/10.1007/BF02803563.

Caffrey, J.M., M.C. Murrell, K.S. Amacker, J.W. Harper, S. Phipps, and M.S. Woodrey. 2014. Seasonal and inter-annual patterns in primary production, respiration, and net ecosystem metabolism in three estuaries in the northeast Gulf of Mexico. *Estuaries and Coasts* 37: 222–241. https://doi.org/10.1007/s12237-013-9701-5.

Carle, M.V., K.G. Benson, and J.F. Reinhardt. 2020. Quantifying the benefits of estuarine habitat restoration in the Gulf of Mexico: An introduction to the theme section. *Estuaries and Coasts* 43: 1680–1691. https://doi.org/10.1007/s12237-020-00807-z.

Carpenter, S.R., S.W. Chisholm, C.J. Krebs, D.W. Schindler, and R.F. Wright. 1995. Ecosystem experiments. *Science* 269: 324–327. https://doi.org/10.1126/science.269.5222.324.

Cloern, J.E. 1987. Turbidity as a control on phytoplankton biomass and productivity in estuaries. *Continental Shelf Research* 7: 1367–1381. https://doi.org/10.1016/0278-4343(87)90042-2.

Cloern, J.E. 1996. Phytoplankton bloom dynamics in coastal ecosystems: A review with some general lessons from sustained investigation of San Francisco Bay, California. *Reviews of Geophysics* 34: 127–168. https://doi.org/10.1029/96RG00986.

Cloern, J.E. 2007. Habitat connectivity and ecosystem productivity: Implications from a simple model. *The American Naturalist* 169: E21–E33. https://doi.org/10.1086/510258.

Cloern, J.E., A.E. Alpine, B.E. Cole, R.L.J. Wong, J.F. Arthur, and M.D. Ball. 1983. River discharge controls phytoplankton dynamics in the northern San Francisco Bay estuary. *Estuarine, Coastal and Shelf Science* 16: 415–429. https://doi.org/10.1016/0272-7714(83)90103-8.

Cloern, J.E., E.A. Canuel, and D. Harris. 2002. Stable carbon and nitrogen isotope composition of aquatic and terrestrial plants of the San Francisco Bay estuarine system. *Limnology and Oceanography* 47: 713–729. https://doi.org/10.4319/lo.2002.47.3.0713.

Cloern, J.E., N. Knowles, L.R. Brown, D. Cayan, M.D. Dettinger, T.L. Morgan, D.H. Schoellhamer, M.T. Stacey, et al. 2011. Projected evolution of California's San Francisco Bay-Delta-River system in a century of climate change. *PLoS ONE* 6: e24465. https://doi.org/10.1371/journal.pone.0024465.

Cloern, J.E., S.Q. Foster, and A.E. Kleckner. 2014. Phytoplankton primary production in the world's estuarine-coastal ecosystems. *Biogeosciences* 11: 2477–2501. https://doi.org/10.5194/bg-11-2477-2014.

Cloern, J.E., A. Robinson, A. Richey, L. Grenier, R. Grossinger, K.E. Boyer, J. Burau, E.A. Canuel, et al. 2016. Primary production in the delta: then and now. *San Francisco Estuary and Watershed Science* 14. https://doi.org/10.15447/sfews.2016v14iss3art1.

Cornwell, J.C., P.M. Glibert, and M.S. Owens. 2014. Nutrient fluxes from sediments in the San Francisco Bay Delta. *Estuaries and Coasts* 37: 1120–1133. https://doi.org/10.1007/s12237-013-9755-4.

Crawford, J.T., L.C. Loken, N.J. Casson, C. Smith, A.G. Stone, and L.A. Winslow. 2015. High-speed limnology: Using advanced sensors to investigate spatial variability in biogeochemistry and hydrology. *Environmental Science & Technology* 49: 442–450. https://doi.org/10.1021/es504773x.

Crosswell, J.R., I.C. Anderson, J.W. Stanhope, B.V. Dam, M.J. Brush, S. Ensign, M.F. Piehler, B. McKee, et al. 2017. Carbon budget of a shallow, lagoonal estuary: Transformations and source-sink dynamics along the river-estuary-ocean continuum. *Limnology and Oceanography* 62: S29–S45. https://doi.org/10.1002/lno.10631.

Doane, T.A., and W.R. Horwáth. 2003. Spectrophotometric determination of nitrate with a single reagent. *Analytical Letters* 36: 2713–2722. https://doi.org/10.1081/AL-120024647.

Domingues, R.B., T.P. Anselmo, A.B. Barbosa, U. Sommer, and H.M. Galvão. 2011. Light as a driver of phytoplankton growth and production in the freshwater tidal zone of a turbid estuary. *Estuarine, Coastal and Shelf Science* 91: 526–535. https://doi.org/10.1016/j.ecss.2010.12.008.

Downing, B.D., B.A. Bergamaschi, C. Kendall, T.E.C. Kraus, K.J. Dennis, J.A. Carter, and T.S. Von Dessonneck. 2016. Using continuous underway isotope measurements to map water residence

time in hydrodynamically complex tidal environments. *Environmental Science & Technology* 50: 13387–13396. https://doi.org/10.1021/acs.est.6b05745.

Eaton, A. D., L. S. Clesceri, A. E. Greenberg, M. A. H. Franson, American Public Health Association, American Water Works Association, and Water Environment Federation. 1998. *Standard methods for the examination of water and wastewater*. Washington, DC: American Public Health Association.

Elser, J.J., M.E.S. Bracken, E.E. Cleland, D.S. Gruner, W.S. Harpole, H. Hillebrand, J.T. Ngai, E.W. Seabloom, et al. 2007. Global analysis of nitrogen and phosphorus limitation of primary producers in freshwater, marine and terrestrial ecosystems. *Ecology Letters* 10: 1135–1142. https://doi.org/10.1111/j.1461-0248.2007.01113.x.

Feyrer, F., S.B. Slater, D.E. Portz, D. Odom, T. Morgan-King, and L.R. Brown. 2017. Pelagic nekton abundance and distribution in the northern Sacramento-San Joaquin Delta, California. *Transactions of the American Fisheries Society* 146: 128–135. https://doi.org/10.1080/00028487.2016.1243577.

Forster, J.C. 1995. Soil nitrogen. In *Methods in Applied Soil Microbiology and Biochemistry*, ed. K. Alef and P. Nannipieri, 79–87. Academic Press.

Frantzich, J., B. Davis, M. MacWilliams, A. Bever, and T. Sommer. 2021. Use of a managed flow pulse as food web support for estuarine habitat. *San Francisco Estuary and Watershed Science* 19. https://doi.org/10.15447/sfews.2021v19iss3art3.

Fregoso, T., A.W. Stevens, R.-F. Wang, T. Handley, P. Dartnell, J.R. Lacy, E. Ateljevich, and E.T. Dailey. 2020. Bathymetry, topography, and acoustic backscatter data, and a digital elevation model (DEM) of the Cache Slough Complex and Sacramento River Deep Water Ship Channel, Sacramento-San Joaquin Delta, California. U.S. Geological Survey data release. https://doi.org/10.5066/P9AQSRVH.

Friedrichs, C.T., and D.G. Aubrey. 1988. Non-linear tidal distortion in shallow well-mixed estuaries: A synthesis. *Estuarine, Coastal and Shelf Science* 27: 521–545. https://doi.org/10.1016/0272-7714(88)90082-0.

Geyer, W.R., J.D. Woodruff, and P. Traykovski. 2001. Sediment transport and trapping in the Hudson River estuary. *Estuaries* 24: 670–679. https://doi.org/10.2307/1352875.

Gross, E., S. Andrews, B. Bergamaschi, B. Downing, R. Holleman, S. Burdick, and J. Durand. 2019. The use of stable isotope-based water age to evaluate a hydrodynamic model. *Water* 11. https://doi.org/10.3390/w11112207.

Hall, R., Jr., and O., and J. L. Tank. 2003. Ecosystem metabolism controls nitrogen uptake in streams in Grand Teton National Park, Wyoming. *Limnology and Oceanography* 48: 1120–1128. https://doi.org/10.4319/lo.2003.48.3.1120.

Hartman, R., S. Bashevkin, A. Barros, C. Burdi, C. Patel, and T. Sommer. 2021. Food for thought: connecting zooplankton science to management in the San Francisco Estuary. *San Francisco Estuary and Watershed Science* 19. https://doi.org/10.15447/sfews.2021v19iss3art1.

Healey, M., P. Goodwin, M. Dettinger, and R. Norgaard. 2016. The state of Bay–Delta science 2016: an introduction. *San Francisco Estuary and Watershed Science* 14. https://doi.org/10.15447/sfews.2016v14iss2art5.

Hoellein, T.J., D.A. Bruesewitz, and D.C. Richardson. 2013. Revisiting Odum (1956): A synthesis of aquatic ecosystem metabolism. *Limnology and Oceanography* 58: 2089–2100. https://doi.org/10.4319/lo.2013.58.6.2089.

Hopkinson, C.S., and E.M. Smith. 2005. Estuarine respiration: an overview of benthic, pelagic, and whole system respiration. In *Respiration in Aquatic Ecosystems*, ed. P. del Giorgio and P. Williams, 122–146. Oxford University Press. https://doi.org/10.1093/acprof:oso/9780198527084.003.0008.

Howarth, R.W., and R. Marino. 2006. Nitrogen as the limiting nutrient for eutrophication in coastal marine ecosystems: Evolving views over three decades. *Limnology and Oceanography* 51: 364–376. https://doi.org/10.4319/lo.2006.51.1_part_2.0364.

Jakobsen, H.H., and S. Markager. 2016. Carbon-to-chlorophyll ratio for phytoplankton in temperate coastal waters: Seasonal patterns and relationship to nutrients. *Limnology and Oceanography* 61: 1853–1868. https://doi.org/10.1002/lno.10338.

Jassby, A.D., J.E. Cloern, and B.E. Cole. 2002. Annual primary production: Patterns and mechanisms of change in a nutrient-rich tidal ecosystem. *Limnology and Oceanography* 47: 698–712. https://doi.org/10.4319/lo.2002.47.3.0698.

Jones, N.L., J.K. Thompson, and S.G. Monismith. 2008. A note on the effect of wind waves on vertical mixing in Franks Tract, Sacramento–San Joaquin Delta, California. *San Francisco Estuary and Watershed Science* 6: Article 4. https://doi.org/10.15447/sfews.2008v6iss2art4.

Kelly, J.R., and S.A. Levin. 1986. A comparison of aquatic and terrestrial nutrient cycling and production processes in natural ecosystems, with reference to ecological concepts of relevance to some waste disposal issues. In *The Role of the Oceans as a Waste Disposal Option*, ed. G. Kullenberg, 300. New York: D. Reidel Publishing Company.

Kemp, M.W., and W.R. Boynton. 1980. Influence of biological and physical processes on dissolved oxygen dynamics in an estuarine system: Implications for measurement of community metabolism. *Estuarine and Coastal Marine Science* 11: 407–431. https://doi.org/10.1016/S0302-3524(80)80065-X.

Kemp, M.W., and W.R. Boynton. 1984. Spatial and temporal coupling of nutrient inputs to estuarine primary production: The role of particulate transport and decomposition. *Bulletin of Marine Science* 35: 522–535.

Kimmerer, W.J. 2004. Open water processes of the San Francisco Estuary: from physical forcing to biological responses. *San Francisco Estuary and Watershed Science* 2. https://doi.org/10.15447/sfews.2004v2iss1art1.

Kimmerer, W.J., and J.K. Thompson. 2014. Phytoplankton growth balanced by clam and zooplankton grazing and net transport into the low-salinity zone of the San Francisco Estuary. *Estuaries and Coasts* 37: 1202–1218. https://doi.org/10.1007/s12237-013-9753-6.

Koseff, J.R., J.K. Holen, S.G. Monismith, and J.E. Cloern. 1993. Coupled effects of vertical mixing and benthic grazing on phytoplankton populations in shallow, turbid estuaries. *Journal of Marine Research* 51: 843–868. https://doi.org/10.1357/0022240933223954.

Kremer, C.T., M.K. Thomas, and E. Litchman. 2017. Temperature- and size-scaling of phytoplankton population growth rates: Reconciling the Eppley curve and the metabolic theory of ecology. *Limnology and Oceanography* 62: 1658–1670. https://doi.org/10.1002/lno.10523.

Lenoch, L., P. Stumpner, J. Burau, L. Loken, and S. Sadro. 2021a. Dispersion and stratification dynamics in the Upper Sacramento River Deep Water Ship Channel. *San Francisco Estuary and Watershed Science* 19: Article 5. https://doi.org/10.15447/sfews.2021v19iss4art5.

Lenoch, L.E.K., L.C. Loken, P.R. Stumpner, S. Sadro, E.E. Van Nieuwenhuyse, J.R. Burau, R.A. Dahlgren, and J. Beaver. 2021b. Nutrient addition experiment in the Sacramento River Deep Water Ship Channel. U.S. Geological Survey data release. https://doi.org/10.5066/P9SKCIUW.

Loken, L.C., E.E. Van Nieuwenhuyse, R.A. Dahlgren, L.E.K. Lenoch, P.R. Stumpner, J.R. Burau, and S. Sadro. 2021. Assessment of multiple ecosystem metabolism methods in an estuary. *Limnology and Oceanography: Methods* 19: 741–757. https://doi.org/10.1002/lom3.10458.

Lopez, C.B., J.E. Cloern, T.S. Schraga, A.J. Little, L.V. Lucas, J.K. Thompson, and J.R. Burau. 2006. Ecological values of shallow-water habitats: Implications for the restoration of disturbed ecosystems. *Ecosystems* 9: 422–440. https://doi.org/10.1007/s10021-005-0113-7.

Lucas, L.V., and E. Deleersnijder. 2020. Timescale methods for simplifying, understanding and modeling biophysical and water quality processes in coastal aquatic ecosystems: A review. *Water* 12: 2717. https://doi.org/10.3390/w12102717.

Lucas, L.V., J.E. Cloern, J.R. Koseff, S.G. Monismith, and J.K. Thompson. 1998. Does the Sverdrup critical depth model explain bloom dynamics in estuaries? *Journal of Marine Research* 56: 375–415. https://doi.org/10.1357/002224098321822357.

Lucas, L.V., D.M. Sereno, J.R. Burau, T.S. Schraga, C.B. Lopez, M.T. Stacey, K.V. Parchevsky, and V.P. Parchevsky. 2006. Intradaily variability of water quality in a shallow tidal lagoon: Mechanisms and implications. *Estuaries and Coasts* 29: 711–730. https://doi.org/10.1007/BF02786523.

Lund, J., E. Hanak, W. Fleenor, W. Bennett, and R. Howitt. 2010. *Comparing futures for the Sacramento, San Joaquin Delta. Comparing Futures for the Sacramento, San Joaquin Delta*. University of California Press. https://doi.org/10.1525/9780520945371.

Mallin, M.A., L.B. Cahoon, M.R. McIver, D.C. Parsons, and G. Christopher Shank. 1999. Alternation of factors limiting phytoplankton production in the Cape Fear River Estuary. *Estuaries* 22: 825–836. https://doi.org/10.2307/1353064.

Malone, T.C., M.W. Kemp, H.W. Ducklow, W.R. Boynton, J.H. Tuttle, and R.B. Jonas. 1986. Lateral variation in the production and rate of phytoplankton in a partially stratified estuary. *Marine Ecology Progress Series* 32: 149–160.

Marineau, M., and S. Wright. 2014. Human alterations of channel characteristics in the delta and effects on hydrodynamics and sediment transport. In: Sediment Dynamics from the Summit to the Sea. In *Proceedings of a symposium held in New Orleans, Louisiana, USA, 11–14 December 2014*, IAHS Publ. 367:11–14. New Orleans, Louisiana, USA.

Martin, J.H., K.H. Coale, K.S. Johnson, S.E. Fitzwater, R.M. Gordon, S.J. Tanner, C.N. Hunter, V.A. Elrod, et al. 1994. Testing the iron hypothesis in ecosystems of the equatorial Pacific Ocean. *Nature* 371: 123–129. https://doi.org/10.1038/371123a0.

Morgan-King, T.L., and D.H. Schoellhamer. 2013. Suspended-sediment flux and retention in a backwater tidal slough complex near the landward boundary of an estuary. *Estuaries and Coasts* 36: 300–318. https://doi.org/10.1007/s12237-012-9574-z.

Murrell, M.C., J.M. Caffrey, D.T. Marcovich, M.W. Beck, B.M. Jarvis, and J.D. Hagy. 2018. Seasonal oxygen dynamics in a warm temperate estuary: Effects of hydrologic variability on measurements of primary production, respiration, and net metabolism. *Estuaries and Coasts* 41: 690–707. https://doi.org/10.1007/s12237-017-0328-9.

Nelson, C.E., A.L. Alldredge, E.A. McCliment, L.A. Amaral-Zettler, and C.A. Carlson. 2011. Depleted dissolved organic carbon and distinct bacterial communities in the water column of a rapid-flushing coral reef ecosystem. *The ISME Journal* 5: 1374–1387. https://doi.org/10.1038/ismej.2011.12.

Platt, T., D.F. Bird, and S. Sathyendranath. 1991. Critical depth and marine primary production. *Proceedings of the Royal Society B* 246: 205–217.

Powell, G.V.N., J.W. Kensworthy, and J.W. Fourqurean. 1989. Experimental evidence for nutrient limitation of seagrass growth in a tropical estuary with restricted circulation. *Bulletin of Marine Science* 44: 324–340.

Qin, Q., and J. Shen. 2021. Typical relationships between phytoplankton biomass and transport time in river-dominated coastal aquatic systems. *Limnology and Oceanography* 66: 3209–3220. https://doi.org/10.1002/lno.11874.

Quay, P.D., D. Wilbur, J.E. Richey, A.H. Devol, R. Benner, and B.R. Forsberg. 1995. The 18O:16O of dissolved oxygen in rivers and lakes in the Amazon Basin: determining the ratio of respiration to photosynthesis rates in freshwaters. *Limnology and Oceanography* 40: 718–729. https://doi.org/10.4319/lo.1995.40.4.0718.

Ragueneau, O., B. Quéguiner, and P. Tréguer. 1996. Contrast in biological responses to tidally-induced vertical mixing for two macrotidal ecosystems of Western Europe. *Estuarine, Coastal and Shelf Science* 42: 645–665. https://doi.org/10.1006/ecss.1996.0042.

Robinson, A., S. Safran, J. Beagle, R. Grossinger, J. Grenier, and R. Askevold. 2014. A delta transformed: ecological functions, spatial metrics, and landscape change in the Sacramento-San Joaquin Delta. Richmond, CA: San Francisco Estuary Institute - Aquatic Science Center.

Schindler, D.W., R.E. Hecky, D.L. Findlay, M.P. Stainton, B.R. Parker, M.J. Paterson, K.G. Beaty, M. Lyng, et al. 2008. Eutrophication of lakes cannot be controlled by reducing nitrogen input: results of a 37-year whole-ecosystem experiment. *Proceedings of the National Academy of Sciences* 105: 11254–11258. https://doi.org/10.1073/pnas.0805108105.

Shrader, K.H., E.L. Zierdt Smith, F. Parchaso, and J.K. McHendrie. 2020. Benthic community and bivalve metrics data in the Sacramento - San Joaquin Delta from 2015 to 2018. U.S. Geological Survey data release. https://doi.org/10.5066/P9JJOL3W.

Sin, Y., R.L. Wetzel, and I.C. Anderson. 1999. Spatial and temporal characteristics of nutrient and phytoplankton dynamics in the York River Estuary, Virginia: Analyses of long-term data. *Estuaries* 22: 260. https://doi.org/10.2307/1352982.

Solomon, C.T., D.A. Bruesewitz, D.C. Richardson, K.C. Rose, M.C. Van de Bogert, P.C. Hanson, T.K. Kratz, B. Larget, et al. 2013. Ecosystem respiration: Drivers of daily variability and background respiration in lakes around the globe. *Limnology and Oceanography* 58: 849–866. https://doi.org/10.4319/lo.2013.58.3.0849.

Sommer, T., C. Armor, R. Baxter, R. Breuer, L. Brown, M. Chotkowski, S. Culberson, F. Feyrer, et al. 2007. The collapse of pelagic fishes in the Upper San Francisco Estuary: El Colapso de los Peces Pelagicos en La Cabecera Del Estuario San Francisco. *Fisheries* 32: 270–277. https://doi.org/10.1577/1548-8446(2007)32[270:TCOPFI]2.0.CO;2.

Stumpner, E.B., B.A. Bergamaschi, T.E.C. Kraus, A.E. Parker, F.P. Wilkerson, B.D. Downing, R.C. Dugdale, M.C. Murrell, et al. 2020a. Spatial variability of phytoplankton in a shallow tidal freshwater system reveals complex controls on abundance and community structure. *Science of the Total Environment* 700: 134392. https://doi.org/10.1016/j.scitotenv.2019.134392.

Stumpner, P.R., J.R. Burau, and A.L. Forrest. 2020b. A Lagrangian-to-Eulerian metric to identify estuarine pelagic habitats. *Estuaries and Coasts*. https://doi.org/10.1007/s12237-020-00861-7.

Sverdrup, H.U. 1953. On conditions for the vernal blooming of phytoplankton. *Journal Du Conseil International Pour L'exploration De La Mer* 18: 287–295.

U.S. Geological Survey. 2020. National Water Information System data available on the World Wide Web (USGS Water Data for the Nation), http://waterdata.usgs.gov/nwis.

Van Nieuwenhuyse, E.E. 2007. Response of summer chlorophyll concentration to reduced total phosphorus concentration in the Rhine River (Netherlands) and the Sacramento – San Joaquin Delta (California, USA). *Canadian Journal of Fisheries and Aquatic Sciences* 64: 1529–1542. https://doi.org/10.1139/f07-121.

Wang, S.R., D. Di Iorio, W.-J. Cai, and C.S. Hopkinson. 2018. Inorganic carbon and oxygen dynamics in a marsh-dominated estuary: Inorganic carbon and oxygen dynamics. *Limnology and Oceanography* 63: 47–71. https://doi.org/10.1002/lno.10614.

Wang, Z., F. Chai, H. Xue, X.H. Wang, Y.J. Zhang, R. Dugdale, and F. Wilkerson. 2021. Light regulation of phytoplankton growth in San Francisco Bay studied using a 3D sediment transport model. *Frontiers in Marine Science* 8: 633707. https://doi.org/10.3389/fmars.2021.633707.

Whipple, A., R.M. Grossinger, D. Rankin, B. Stanford, and R.A. Askevold. 2012. Sacramento-San Joaquin Delta historical ecology investigation: exploring pattern and process. *SFEI Contribution* No. 672.

Wilkerson, F.P., R.C. Dugdale, A.E. Parker, S.B. Blaser, and A. Pimenta. 2015. Nutrient uptake and primary productivity in an urban estuary: Using rate measurements to evaluate phytoplankton response to different hydrological and nutrient conditions. *Aquatic Ecology* 49: 211–233. https://doi.org/10.1007/s10452-015-9516-5.

Winslow, L.A., J. Read, and R. Woolway. 2019. *rLakeAnalyzer: lake physics tools* (version R package version 1.11.4.1).

Xu, J., K. Yin, J.H.W. Lee, D.M. Anderson, Y. Jiang, X. Yuan, A.Y.T. Ho, and P.J. Harrison. 2012. Resistance of Hong Kong waters to nutrient enrichment: Assessment of the role of physical processes in reducing eutrophication. *Journal of Oceanography* 68: 545–560. https://doi.org/10.1007/s10872-012-0118-8.

Yin, K., and P. Harrison. 2000. Influences of flood and ebb tides on nutrient fluxes and chlorophyll on an intertidal flat. *Marine Ecology Progress Series* 196: 75–85. https://doi.org/10.3354/meps196075.

Yin, K., P.J. Harrison, R.H. Goldblatt, and M. A. St.John, and R. J. Beamish. 1997. Factors controlling the timing of the spring bloom in the Strait of Georgia Estuary, British Columbia, Canada. *Canadian Journal of Fisheries and Aquatic Sciences* 54: 1985–1995. https://doi.org/10.1139/f97-106.

Yoshiyama, K., and J.H. Sharp. 2006. Phytoplankton response to nutrient enrichment in an urbanized estuary: Apparent inhibition of primary production by overeutrophication. *Limnology and Oceanography* 51: 424–434. https://doi.org/10.4319/lo.2006.51.1_part_2.0424.

Young, M.J., F. Feyrer, P.R. Stumpner, V. Larwood, O. Patton, and L.R. Brown. 2020. Hydrodynamics drive pelagic communities and food web structure in a tidal environment. *International Review of Hydrobiology*. https://doi.org/10.1002/iroh.202002063.

Zierdt Smith, E.L., K.H. Shrader, F. Parchaso, and J.K. McHendrie. 2021. Benthic communities as mediators of water quality in Lower San Francisco Bay, California (2012–2019). U.S. Geological Survey data release. https://doi.org/10.5066/P98VDE7V.